ACS APPLIED MATERIALS & INTERFACES

Research Article

Cite This: ACS Appl. Mater. Interfaces 2019, 11, 28699−28719

www.acsami.org

TiCaPCON-Supported Pt- and Fe-Based Nanoparticles and Related Antibacterial Activity

Viktor A. Ponomarev,[†] Aleksander N. Sheveyko,[†] Elizaveta S. Permyakova,[†] Jihyung Lee,[‡] Andrey A. Voevodin,[‡] Diana Berman,[‡] Anton M. Manakhov,[†] Miroslav Michlíček,[§,∥] Pavel V. Slukin,[⊥] Viktoriya V. Firstova,[⊥] Sergey G. Ignatov,[⊥] Ilya V. Chepkasov,[†,#] Zakhar I. Popov,[†,¶] and Dmitry V. Shtansky*[,†]

[†]National University of Science and Technology "MISIS", Leninsky prospect 4, Moscow 119049, Russia

[‡]Department of Materials Science and Engineering, University of North Texas, Denton, Texas 76203, United States

[§]Plasma Technologies, CEITEC - Central European Institute of Technology, Masaryk University, Kotlářská 2, Brno 61137, Czech Republic

[∥]Department of Physical Electronics, Faculty of Science, Masaryk University, Kotlářská 2, Brno 61137, Czech Republic

[⊥]State Research Center for Applied Microbiology and Biotechnology, Obolensk, Moscow Region 142279, Russia

[#]Katanov Khakas State University, Abakan 655017, Russia

[¶]Emanuel Institute of Biochemical Physics RAS, Moscow 199339, Russia

Supporting Information

ABSTRACT: A rapid increase in the number of antibiotic-resistant bacteria urgently requires the development of new more effective yet safe materials to fight infection. Herein, we uncovered the contribution of different metal nanoparticles (NPs) (Pt, Fe, and their combination) homogeneously distributed over the surface of nanostructured TiCaPCON films in the total antibacterial activity toward eight types of clinically isolated bacterial strains (*Escherichia coli* K261, *Klebsiella pneumoniae* B1079k/17-3, *Acinetobacter baumannii* B1280A/17, *Staphylococcus aureus* no. 839, *Staphylococcus epidermidis* i5189-1, *Enterococcus faecium* Ya-235: VanA, *E. faecium* I-237: VanA, and *E. coli* U20) taking into account various factors that can affect bacterial mechanisms: surface chemistry and phase composition, wettability, ion release, generation of reactive oxygen species (ROS), potential difference and polarity change between NPs and the surrounding matrix, formation of microgalvanic couples on the sample surfaces, and contribution of a passive oxide layer, formed on the surface of films, to general kinetics of the NP dissolution. The results indicated that metal ion implantation and subsequent annealing significantly changed the chemistry of the TiCaPCON film surface. This, in turn, greatly affected the shedding of ions, ROS formation, potential difference between film components, and antibacterial activity. The presence of NPs was critical for ROS generation under UV or daylight irradiation. By eliminating the potential contribution of ions and ROS, we have shown that bacteria can be killed using direct microgalvanic interactions. The possibility of charge redistribution at the interfaces between Pt NPs and TiO_2 (anatase and rutile), TiC, TiN, and TiCN components was demonstrated using density functional theory calculations. The TiCaPCON-supported Pt and Fe NPs were not toxic for lymphocytes and had no effect on the ability of lymphocytes to activate in response to a mitogen. This study provides new insights into understanding and designing of antibacterial yet biologically safe surfaces.

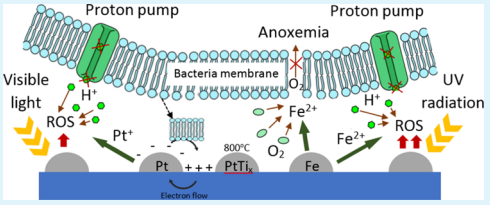

KEYWORDS: *antibacterial films, bactericide ion release, reactive oxygen species, electrochemical behavior, Kelvin probe force microscopy, microgalvanic effect*

1. INTRODUCTION

The development of an efficient and reliable technology of surface modification is critical to reducing the overall rate of implant-related bacterial infection. For orthopedic and dental implants, two main functions are simultaneously required: preventing infection and promoting osseointegration.[1] The implant surface should be endowed with bactericidal activity against pathogenic microorganisms but remain inactive for symbiotic bacteria. Because the surface of metals and alloys is bioinert, surface modification is often aimed at imparting materials with bioactive properties to improve osseointegration. There are several main competing strategies against pathogenic bacterial and fungal infections: (i) doping with bactericidal ions,[2,3] (ii) fabrication of heterogeneous surfaces decorated with

Received: June 5, 2019
Accepted: July 24, 2019
Published: July 24, 2019

DOI: 10.1021/acsami.9b09649
ACS Appl. Mater. Interfaces 2019, 11, 28699−28719

Table 1. Ion Implantation and Annealing Parameters

sample	first cycle					second cycle				
	cathode	voltage, kV	current, mA	time, min	annealing temperature, °C	cathode	voltage, kV	current, mA	time, min	annealing temperature, °C
Pt	Pt	30	7	60						
Pt_{an}	Pt	30	7	60	700					
Pt_{an} + Fe	Pt	30	7	60	700	Fe	25	5	15	
Pt + Fe	Pt	30	7	60		Fe	25	5	15	
$(Pt + Fe)_{an}$	Pt	30	7	60		Fe	25	5	15	700
Fe	Fe	30	5	60						
Fe_{an}	Fe	30	5	60	700					

bactericidal metal nanoparticles (NPs),[4−6] (iii) grafting of different antibiotics, antibacterial peptides, quaternary ammonium and phosphonium compounds, anticoagulants, and NO radicals to the surfaces,[6−8] and (iv) design of specific surface topography and roughness.[9−12] The challenges brought by the bacterial contamination of implant surfaces and different approaches to kill or restrain bacterial culture growth and prevent infection were recently reviewed.[13−15] Because bacteria differ in shape, size, cell wall thickness, outer membrane composition, and many other characteristics, the causes of their death can also be different. When placed in the human body, the implant surface can (i) inhibit bacterial adhesion and biofilm formation because of the electrostatic interaction with bacteria (the so-called anti-adhesion, bacterial-repelling, or antifouling surface), (ii) release bactericide ions that kill bacteria through one or more known mechanisms (damage of cell envelope and cytoplasmic component, blocking the peptidoglycan ability to transfer oxygen, inactivation of enzymatic functions of proteins, and disrupting the DNA replication), (iii) generate reactive oxygen species (ROS) that cause oxidative stress in bacteria, and (iv) induce significant galvanic coupling between spherical metal precipitates and surrounding ceramic matrix and kill bacteria through direct microgalvanic interactions.

Despite significant progress in the field of antibacterial films, there is currently no clear understanding of what is the main cause of the death of a specific type of bacteria. In addition, many popular approaches for antibacterial surface design, for example, Ag ion-based strategy or grafting/loading antibiotics, require very careful optimization of the bactericide component to avoid material toxicity. Antibiotics can be immobilized on the implant surface, but the success of this strategy depends on the ability of the antibiotic to remain functional in its tethered form.[16−18] The available results regarding the concentration of bactericidal ions required for bacterial deactivation are rather contradictive.[19] For example, Vaidya et al.[20] reported minimal bactericidal concentrations for five types of bactericidal ions (Ag, Cu, Pt, Au, and Pd) against three types of bacteria (*Klebsiella pneumoniae* (*K. pneumoniae*), *Acinetobacter baumannii* (*A. baumannii*), and *Enterococcus faecium* (*E. faecium*)) that were in the parts per million (ppm) range, whereas numerous studies demonstrated a noticeable antibacterial effect for substantially lower bactericide ion concentrations in the parts per billion (ppb) range.[11,21] Ag-doped films were reported to demonstrate a fast and pronounced antibacterial effect at a very low Ag ion concentration of 0.1−0.3 ppb.[22] Heavy metals (Cr, Co, Cu, Au, Fe, Ni, Pt, Ag, Ta, etc.) are being present naturally in the environment,[23] but in large amount, they can be toxic.[24] For example, the toxic effect of Ag^+ ions adsorbed on cell walls resulting in their damage was reported in many studies.[25,26] To this end, most works in this field were aimed at imparting the antibacterial activity to the specific material, but only a few scientific investigations considered factors affecting bactericidity toward different bacteria.

The design of proper nano-biosurfaces is a promising approach toward the fabrication of biocompatible yet antibacterial materials. The present study intends to explore the role of metal NPs in the antibacterial properties of TiCaPCON-based films. These multicomponent bioactive nanostructured films were selected because they had recently passed clinical studies and were approved for medical applications.[27] To address this important issue, three main types of samples with Pt, Fe, and Pt + Fe NPs on the surface of TiCaPCON films (hereafter denoted as Pt, Fe, and Pt + Fe) were obtained by a combination of magnetron sputtering and metal ion implantation. Additionally, several samples were annealed in vacuum either before or after ion implantation to change the surface chemistry, NP size, and their surface distribution. Thus, additional four sample groups were fabricated, hereafter denoted as Pt_{an}, Fe_{an}, Pt_{an} + Fe, and $(Pt + Fe)_{an}$. The samples were tested toward eight types of clinically isolated bacterial strains (antibiotic-resistant *Escherichia coli* (*E. coli*) K261, *K. pneumoniae* B1079k/17-3, *A. baumannii* B1280A/17, *Staphylococcus aureus* (*S. aureus*) no. 839, *Staphylococcus epidermidis* (*S. epidermidis*) i5189-1, *E. faecium* Ya-235: VanA, *E. faecium* I-237: VanA, and antibiotic-sensitive *E. coli* U20). To elucidate possible antibacterial mechanisms, the following factors were taken into account: surface chemistry and phase composition, wettability, ion release, ROS generation, potential difference and polarity change between NPs and the surrounding matrix, formation of microgalvanic couples on the sample surfaces, and contribution of a passive oxide layer, formed on the surface of films, to general kinetics of NP dissolution. Quantum chemical modeling within the framework of density functional theory (DFT) was performed to support the observed results. To exclude the possible toxic issue, immunomodulation of Pt- and Fe-implanted TiCaPCON films on immune cells was also carried out.

2. MATERIALS AND METHODS

2.1. Deposition of TiCaPCON Films. The TiCaPCON films, 0.8−1.0 μm thick, were deposited by dc magnetron sputtering of TiC−CaO−Ti_3PO_x target (120 mm in diameter and 8 mm in thickness) obtained by the self-propagating high-temperature synthesis method. According to the energy-dispersive spectroscopy (EDS) data, the target elemental composition was Ti—52.7, Ca—1.1, P—1.5, C—30.6, O—4.3, and N—9.8 (at. %). Single-crystal silicon wafer (100) was used as the substrate material. The distance from the target to the substrate was 100 mm. First, the vacuum chamber was evacuated to a pressure of 10^{-3} Pa and then filled with Ar to a total pressure of 0.2 Pa. Before deposition, the substrates were ion-cleaned for 10 min using an additional 3 keV Ar ion source, ensuring a substrate current density of 2

DOI: 10.1021/acsami.9b09649
ACS Appl. Mater. Interfaces 2019, 11, 28699−28719

mA/cm^2. To enhance film adhesion, the Si substrates were treated with Ti^{2+} ions with energy 60 kV for 7 min before and 5 min after the beginning of deposition using a MEVVA-type ion implanter. During deposition, the magnetron current was set to 2 A (Advanced Energy Pinnacle Plus unit), the total pressure in the vacuum chamber was maintained at 0.1 Pa, and the substrate bias voltage was kept constant at −50 V. The deposition process was carried out in a gaseous mixture of Ar and N_2 with a nitrogen partial pressure of $N_2/(N_2 + Ar) = 15\%$ for 20 min.

2.2. Ion Implantation. Pt and Fe ions were implanted into the TiCaPCON films using metal cathodes (99.99%) on the MEVVA-type ion implanter. Samples were fixed with the film-coated side in the direction of the suppressor mesh. The ion implantation experiments were carried out in an Ar atmosphere at a pressure of 2×10^{-2} Pa. The pulse frequency of the arc discharge was 20 Hz, the accelerating voltage was set at 30 kV, and the current was maintained in the range of 5−7 mA (Table 1). First, Pt and Fe ions were implanted into the TiCaPCON films either separately or consecutively for 60 min to form Pt, Fe, and Pt + Fe samples. Then, a part of samples was annealed in vacuum under a pressure of 10^{-3} Pa at a temperature of 700 °C for 1 h (samples hereafter referred to as Pt_{an}, Fe_{an}, and $(Pt + Fe)_{an}$). Finally, the Pt_{an} film was implanted with Fe ions using the regime described above. All seven sample types are depicted in Table 1.

2.3. Film Characterization. The film microstructure was examined by scanning electron microscopy (SEM) using a JSM-7600F instrument (JEOL, Japan). The specimens for transmission electron microscopy (TEM) study were prepared using a Helios 600i DualBeam system (Thermo Fisher Scientific). High-resolution TEM (HRTEM) analysis was carried out on a C_s-corrected Titan 80-300 platform (Thermo Fisher Scientific) equipped with an energy-dispersive X-ray (EDX) detector. The surface chemical composition and valence states were studied by X-ray photoelectron spectroscopy (XPS) using an Axis Supra spectrometer (Kratos Analytical, UK). The XPS measurements were carried out with a charging neutralizer from an area of 0.38 mm^2 in steps of 20 eV, and the obtained XPS spectra were further analyzed with the shifting of the binding energy (BE) scale to obtain the position of C 1s peak at 285.0 eV (for the samples without graphite contribution) and 284.4 eV (for the samples with graphite). The fitting of XPS spectra was done with the CasaXPS software after the subtraction of the Shirley-type background employing Gaussian−Lorentzian (G−L) peaks with the fixed G−L percentage of 30 for a majority of the peaks. The metallic Pt peaks and graphite C 1s peak were fitted using an asymmetric LF function embedded into CasaXPS software. Raman analysis was performed on a Nicolet Almega XR Dispersive Raman spectrometer with a 532 nm green laser. Specular reflectance IR (SR-IR) spectra were recorded in a Cary-5000 spectrophotometer equipped with UMA accessory within the wavelength of 200−1000 nm. Measurements were carried out in the two-beam mode using the partially polarized light at an incidence angle of 30, 40, 50, and 60 degree.

2.4. Atomic Force Microscopy and Kelvin Probe Force Microscopy. The surface modification experiments were performed using the Bruker Multimode 8 (Bruker, USA) atomic force microscope in the amplitude modulation Kelvin probe force microscopy mode. The surface modifications were analyzed after immersing the samples in the normal saline solution (NSS, 0.9 wt % of NaCl in water). For this, the samples kept in a beaker with the solution were rinsed with deionized water and grounded with a silver paste to the metal specimen support. During the measurements, the distance between the sample and the probe was 70 nm. The scanning speed was 0.5 Hz (5 μm/s).

2.5. Wettability. Static water contact angle values of the samples were measured in the ambient environment by the sessile drop method using distilled water drops, 3 μL volume, with a CAM 101 optical contact angle meter (KSV) equipped with a video-imaging system. For each sample, the contact angles were analyzed in dynamics after 0, 5, and 10 min, and the results were averaged based on five measurements.

2.6. Electrochemical Tests. Electrochemical studies were carried out in NSS (0.9% NaCl) at a temperature of 25 ± 0.1 °C using a Voltalab PST050 potentiostat (Radiometer Analytical). The measurements were performed in a thermostated electrochemical cell equipped with an AgCl reference electrode and a Pt auxiliary electrode with an area (S) of 1 × 1 cm^2. The coated Si samples, 20 × 15 mm^2 in size, were varnished, leaving a window of 1 × 1 cm^2 for interaction with the electrolyte, and fixed on a special copper holder. The electric contact was applied to the coating via a copper clamp with a wire soldered to it. The sample was suspended in the electrolyte cell to ensure that the clamp was above the solution surface. Two types of tests were carried out. First, open-circuit corrosion potentials (OCPs) were measured for 30 min. All potentials were recalculated for a standard hydrogen reference electrode (the potentials were shifted by 199 mV). Second, polarization curves were obtained starting from the potential being more negative than OCP to the potential of 3.0 V with a rate of 3 mV/s.

2.7. Ion Release. The rate of metal ion release was determined by inductively coupled plasma mass spectroscopy (ICP-MS) using an X-Series II instrument (Thermo Fisher Scientific, USA). Square samples (1 cm^2) were immersed in flasks filled with 20 mL of NSS kept at room temperature. Aliquots (1.5 mL) were collected after 1, 3, 6, 12, 24, 48, and 72 h to analyze the concentration of ions released over the experiment time. For every collected sample, the concentration of ions was recalculated for the remaining volume.

2.8. Reactive Oxygen Species. The 2′,7′-Dichlorohydrofluorescein diacetate assay ($DCFH_2$-DA) was used to quantitate ROS.[28] $DCFH_2$ was prepared from $DCFH_2$-DA by mixing 0.5 mL of 1.0 mM DCFH-DA in dimethyl sulfoxide with 2.0 mL of 0.01 N NaOH. The deesterification of DCFH-DA proceeded at room temperature for 30 min and then the mixture was neutralized with 10 mL of NaH_2PO_4 (25 mM, pH 7.4). To construct a calibration curve, several solutions with a different concentration of $DCFH_2$ (1, 10, 100, and 1000 nM) in 40 mM Tris buffer at pH 7.4 were prepared. The solutions were treated with a mixture containing H_2O_2 (10 μM) + Fe^{2+} (10 μM) {from $FeSO_4$}.[29] The samples were analyzed using a Cary Eclipse fluorescence spectrophotometer (Agilent Technologies) using excitation 495 nm and emission 520 nm wavelengths.[30] To determine the ROS amount, the samples (S = 1 × 1 cm^2) were immersed in 10 mL of NSS. A pH value during ROS measurements was 7.4. After 1, 3, 12, and 24 h, 3 mL of aliquots was collected for reaction with $DCFH_2$-DA and ROS quantification. Different fluorescence spectrophotometry tests were carried out after sample exposure under UV (30 min) and visible light (8 h) irradiation and after the storage in the dark for 8 h. The films were UV-irradiated with an ANC 170/70-P3-3 germicidal lamp (LIT Phonon) at a wavelength of 253.7 nm and a power of 50 W. The distance between the lamp and the samples was set at 10 cm. For visible light irradiation, the samples were placed on the windowsill from 10 a.m to 6 p.m. To study the ROS recombination, the ROS concentration was measured after 54−66 h of aliquot storage. In addition, several samples were preliminarily kept in NSS for 24 h, then the solution was replaced with a new one, and finally the ROS concentration was measured after 8 h.

2.9. Immunomodulation of Pt- and Fe-Implanted NPs on Immune Cells. *2.9.1. Cell Cultures.* To assess the cytotoxicity of Pt- and Fe-implanted NPs, the viability, the proliferation of lymphocyte, as well as the expression of activation markers CD69 and CD25 on the lymphocyte surface were studied. Heparinized blood, diluted 2-fold with phosphate-buffered saline (PBS) with 2% fetal bovine serum (FBS), was layered on a Histopaque-1077 density gradient (Sigma, USA) in a ratio of 1:1 and centrifuged with the acceleration of 400g at room temperature for 30 min. The selected opalescent ring was washed twice at 250g in 10 mL of PBS with 2% PBS. The pellet was resuspended in RPMI 1640 complete nutrient medium containing 10% FBS, 2 mM glutamine (PanEco, Russia), 10 mM 4-(2-hydroxyethyl)-1-piperazineethanesulfonic acid (Sigma, USA), and 25 μM 2-mercaptoethanol (Sigma, USA). Cell viability was determined using a trypan blue assay. The concentration of cell suspension was adjusted to 10^6 cells/mL using an automatic TC-20 counter (Bio-Rad, USA).

2.9.2. Cytotoxicity Tests. After separation on a density gradient, lymphocytes were incubated in the presence of test samples in full nutrient medium RPMI 1640 and 5% CO_2 at 37 °C for 7 days. Lymphocyte viability was determined daily using the vital 7-aminoactinomycin D (7-AAD) intercalating DNA dye, which penetrates into the cell only when the integrity of the membrane is broken. The as-prepared 7-AAD solution (5 μL) was added to the

DOI: 10.1021/acsami.9b09649
ACS Appl. Mater. Interfaces 2019, 11, 28699−28719

mononuclear cell suspension (10^6 cells/mL) selected on the density gradient and incubated for 10 min. Samples were analyzed after 15 min staining on a FACSAria III flow cytometer (Becton Dickinson, USA) using BD FACSDiva software (version 8.0). Cells (10^4) were analyzed in each sample.

2.9.3. Cell Proliferation Assay. The proliferation of lymphocytes was determined using the carboxyfluorescein (CFSE) dye. When a CFSE-labeled cell divides, its progeny is endowed with half the number of CFSE-tagged molecules and thus each cell division can be assessed by measuring the corresponding decrease in cell fluorescence via flow cytometry. The more of cell divisions (mitoses) occurred, the lower the level of luminescence. On the cytometric histogram, the CFSE-stained cells are arranged in a series of consecutive peaks with decreasing luminescence intensity.

Lymphocytes (10^6 cells/mL) were stained with 5 mM CFSE prior to their cultivation (BD e-Bioscience, USA). Cells were incubated with CFSE (showing high initial luminescence intensity) and/or a mitogen ConA (10 μg/mL) in the presence of test samples in an atmosphere of 5% CO_2 at 37 °C for 10 min. Then, 3 mL of cooled RPMI-1640 medium was added, incubated in the cold for 5 min, and then washed twice with cooled RPMI-1640 containing 10% FBS. Centrifugation was carried out at an acceleration of 400*g* for 5−7 min. The cells were resuspended in RPMI-1640-based complete nutrient medium to their original concentration. Then, the cell suspension was introduced into the wells of a 96-well plate and incubated with test samples and/or a mitogen ConA (10 μg/mL) in 5% CO_2 at 37 °C for 6 days renewing the medium, if necessary. At the end of incubation, the cell suspension was transferred into cytometric tubes and then 1 mL of PBS was added. After centrifugation at 400*g* for 5 min, the supernatant was removed, resuspended, fixed with 1% formalin solution, and finally analyzed using flow cytometry method.

2.9.4. Immune Cell Activation Analysis. After separation on a density gradient, lymphocytes were incubated in the presence of test films in full nutrient medium RPMI 1640 and 5% CO_2 at 37 °C for 2 days. Then, the lymphocytes were phenotyped. For this, the lymphocyte suspension (10^6 cells/mL) was stained with monoclonal antibodies (eBioscience, USA): CD3 PerCP-Cy 5.5 (to identify T-cells), CD19 PE (B-cells), and CD25 APC and CD 69 FITC (to reveal the activation markers on the surface of T- and B-lymphocytes). Staining was carried out in the dark at 20 °C for 20 min. Then, the cells were washed in PBS, fixed with 1% formalin solution, and subjected to flow cytometry analysis within 24 h. In each sample, 10^4 cells were analyzed on an FACSAria III flow cytometer (Becton Dickinson, USA) using BD FACSDiva software (version 8.0).

2.10. Antibacterial Activity. Before tests, all samples were sterilized by UV radiation from a distance of 150 mm for 30 min. The test samples were placed into the wells of a sterile 24-well culture plate (Sigma-Aldrich) filled with 0.5 mL of NSS. A sample-free well and a well with NP-free TiCaPCON sample were used as controls. Simultaneously, 0.03 mL of the overnight culture suspension of test strains in NSS was added to all wells with a cell concentration of about 10^4−10^5 CFU/mL. The samples were incubated in a thermostat at 37 °C. Aliquots of 0.04 mL were taken for each sample at different intervals (typically 3, 8, and 24 h).

To reveal how NPs affect the early stage of biofilm formation, the samples were removed from each well, washed twice in 10 mL of NSS, and finally sonicated in 5 mL of NSS on a Soniprep 150 homogenizer (MSE Ltd, UK) with an amplitude of 2 μm for 2 min. The obtained bacterial suspensions were used to determine the concentration of colony forming units (CFUs).

To obtain CFU concentrations, the content of each well was titrated using a serial 10-fold bacterial dilution on 0.3 mL of NSS. From each dilution, 0.01 mL of bacterial suspension was sown on Petri dishes with a nutrient medium Mueller Hinton Agar (HiMedia, India), dried in a closed dish at room temperature for 10 min, incubated in the thermostat at 37 °C for 24 h, and then the culture titer was counted. The experiments were performed in triplicate, and the statistic calculations were performed using the Data Analysis Tool of Microsoft Office, Excel 2010 (Microsoft Corp.).

2.11. Modeling. Quantum chemical modeling was performed within the framework of DFT[31,32] using plane wave basis set and the PAW method[33,34] as implemented in VASP.[35−37] Generalized gradient approximation was used in the form of Perdew−Burke−Ernzerhof exchange−correlation functional.[38] For the Brillouin zone sampling, gamma-centered Monkhorst−Pack scheme[39] was chosen with a *k*-point mesh which depends on cell size. The plane wave basis cutoff energy E_{cutoff} = 400 eV was used. The van der Waals interactions were taken into consideration.[40] In all geometry optimizations, the convergence criterion was such that the maximal force acting on any atom was less than 0.01 eV/Å. The Bader approach[41] was used in order to calculate the atomic charge based on the VASP results. All structures were visualized in VESTA.[42]

3. RESULTS

3.1. TiCaPCON Films. The structure and elemental composition of TiCaPCON films were previously studied in detail,[22] and for the convenience of readers, they are described here only briefly. The films revealed small TiCN grains, 6−15 nm in size, surrounded by an amorphous matrix containing Ca, P, and O. According to the EDS analysis, the film elemental composition was Ti—43.3, C—31.5, N—15.4, O—8.2, and Ca—1.6 at. %.

3.2. Scanning Electron Microscopy. Figure 1 shows the top view SEM images of the TiCaPCON films after different surface treatments. Pt ion implantation led to the formation of Pt NPs, 15−30 nm in size, located on the TiCaPCON film surface (Figure 1a). At the accelerating voltage of 30 kV, metallic ions were reported to penetrate TiCaPCON films to a depth up to 30−40 nm.[19] After sample annealing in vacuum at 700 °C for 1 h, NP density significantly increased because of Pt atom diffusion from depth to surface, whereas the NP size has not changed (Figure 1b). The Fe-implanted sample reveals only single Fe NPs on its surface whose size did not exceed 5−7 nm (Figure 1c). Further annealing resulted in the precipitation and growth of shapeless Fe NPs (Figure 1d). In the case of the sequential Pt + Fe ion implantation, the NP size and distribution were similar to that of the Pt sample (Figure 1e). After annealing, the size of large NPs remained unchanged but NP density

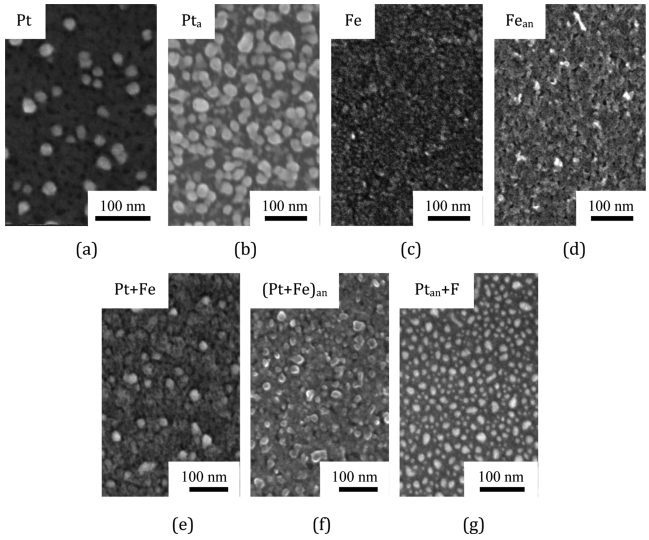

Figure 1. SEM surface images of TiCaPCON films after different surface treatments. (a) Pt ion implantation (II), (b) Pt II + annealing, (c) Fe II, (d) Fe II + annealing, (e) subsequent Pt and Fe II, (f) subsequent Pt and Fe II + annealing, and (g) Pt II + annealing + Fe II.

DOI: 10.1021/acsami.9b09649
ACS Appl. Mater. Interfaces 2019, 11, 28699−28719

increased because of the precipitation of smaller NPs (Figure 1f). The surface of Pt_{an} + Fe film was densely populated with small NPs being 3−20 nm in diameter (Figure 1g).

3.3. Transmission Electron Microscopy. Figure 2 shows the cross-sectional TEM and HRTEM images of the Pt + Fe

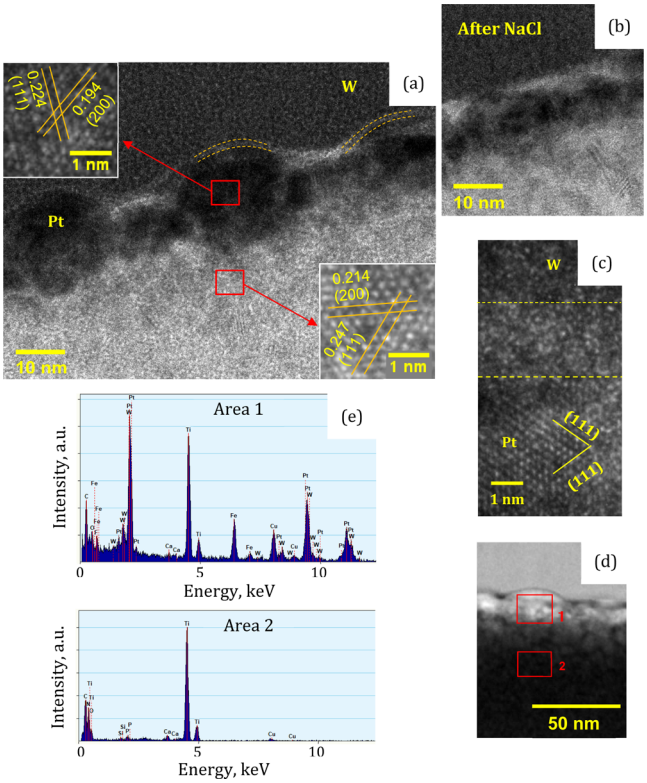

Figure 2. TEM (a,b,d) and HRTEM [a, insets, c] images of Pt + Fe samples before (a,d) and after immersion in NSS for 24 h (b,c) and corresponding EDX spectra (e) of the selected areas shown in (d).

sample taken before and after exposure in NSS for 24 h. A thin subsurface layer (~20 nm) with Pt NPs is clearly seen (Figure 2a). The HRTEM images revealed characteristic planes of the Pt and TiC phases in the film (Figure 2a,insets). A thin amorphous surface layer (~1−1.5 nm) was also observed. The EDX spectroscopy analysis confirmed that the thin subsurface layer is enriched with Pt and Fe (Figure 2e). Below the implanted layer, only Ti, Ca, P, C, O, and N elements were detected (a Cu signal came from the specimen holder). After sample exposure in NSS, the thickness of the ion-implanted layer was observed to decrease (Figure 2b) because of the ion release process, as described in Section 3.7. Simultaneously, the thickness of the amorphous oxide layer increased to 2.5 nm (Figure 2c) because of the surface passivation (see Section 3.10). The Fe-rich phases were not detected, probably because of the formation of Pt−Fe solid solution.[43]

3.4. XPS (before Immersion in NSS). The XPS spectra of all seven types of TiCaPCON-based samples decorated with metallic NPs were recorded. As an example, full survey XPS spectra of Fe, Pt, and Pt_{an} samples before and after immersion in NSS are presented in Figure S1. They demonstrate the absolute heights of the XPS peaks of different elements, thereby showing how much of the underlying TiCaPCON layer is seen by XPS.

The characteristic high-resolution XPS C 1s spectra of Fe, Pt, Pt_{an}, Pt + Fe, and Pt_{an} + Fe samples were fitted using three components: amorphous carbon (hydrogenated a-CH_x and a-C (x = 0) phases have similar BE ≈ 285 eV, full width at half-maximum (fwhm) = 1.35 ± 0.1 eV), C═O (BE = 288.1 ± 0.2 eV, fwhm ≈ 2 eV), and C−O (BE = 286.4 ± 0.2 eV, fwhm = 1.5 ± 0.2 eV), which are presented in Figures 3 and S2. The titanium carbide bonding contribution Ti−C (BE = 282 ± 0.2 eV, fwhm = 1.0 ± 0.1 eV) was visible in the Fe_{an} (Figure S2b) and Pt + Fe (Figure 3c) films, but its concentration was below 2%. In the Pt- and Fe-implanted samples after annealing [Pt_{an}, $(Pt + Fe)_{an}$, and Fe_{an}], the characteristic C−C (graphite) peak at 284.4 eV[44] instead of a-C at 285 eV was observed (Figures 3b,d and S2b, respectively). Carbon materials with graphite structure have the characteristic asymmetric XPS C 1s peak shape with a long tailing component in the higher BE side.[45] These graphite satellite feature is well seen at 290−292 eV (Figures 3d, inset, and S2b). The absence of graphite peak in the Pt_{an} + Fe sample can be explained by sputtering a thin top layer during the Fe ion implantation. The formation of the graphite phase was also confirmed by Raman spectroscopy. As an example, Figure 3e,f compares the Raman spectra of the Pt + Fe and $(Pt + Fe)_{an}$ samples. Both spectra revealed two features because of the relative motion of sp^2 carbon atoms (G peak) and breathing modes of rings (D peak). It can be seen that after annealing, the G peak shifted from 1480 to 1515 cm^{-1} and the intensity of D peak significantly increased, thereby indicating a-C to nanocrystalline graphitic carbon transformation during annealing.[46]

Before annealing, the Fe and Pt + Fe films revealed two components in their XPS N 1s spectra: TiN (BE ≈ 397 eV, fwhm = 1.7 ± 0.2 eV) and N−C═O (BE = 399.9 ± 0.2 eV, fwhm = 1.5 ± 0.2 eV) (Figure S3). After annealing [Fe_{an} and $(Pt + Fe)_{an}$ samples], the contribution of the N−C═O component significantly decreased. The N 1s peak of the Pt sample required the addition of a third component, namely, C−N (BE = 399.2 eV, fwhm = 1.6 eV). After heat treatment, all three components (TiN, C−N, and N−C═O) were observed to contribute in the corresponding XPS N 1s spectra of the Pt_{an} and Pt_{an} + Fe films.

The Pt environment was evaluated from the curve-fitting of Pt $4f_{7/2}$ and $4f_{5/2}$ signals using four components (Figures 4 and S2d): two main peaks from metallic Pt ($BE_{4f\ 7/2}$ = 71.0 ± 0.1 eV $fwhm_{4f\ 7/2}$ = 1.0 ± 0.1 eV; $BE_{4f\ 5/2}$ = 74.2 ± 0.1 eV $fwhm_{4f\ 5/2}$ = 1.1 ± 0.1 eV) and Pt−Ti ($BE_{4f\ 7/2}$ = 71.5 ± 0.1 eV $fwhm_{4f\ 7/2}$ = 0.9 ± 0.1 eV; $BE_{4f\ 5/2}$ = 74.7 ± 0.1 eV $fwhm_{4f\ 5/2}$ = 1.0 ± 0.1 eV) compound, and minor contributions from Pt oxide (PtO, $BE_{4f\ 7/2}$ = 73.0 eV $fwhm_{4f\ 7/2}$ = 1.2 eV; $BE_{4f\ 5/2}$ = 75.7 eV $fwhm_{4f\ 5/2}$ = 1.1 ± 0.1 eV). After annealing, the Pt $4f_{5/2}$ and $4f_{7/2}$ peaks shift approximately 0.4 eV to higher BE and the relative intensity of the Pt−Ti and PtO peaks considerably increased (Pt_{an} sample). A similar shift was observed in binary Pt/Ti films after annealing as attributed to the formation of $TiPt_3$ phase.[47] Moreover, new contribution of PtO_2 was revealed ($BE_{4f\ 5/2}$ = 76.4 eV, $fwhm_{4f\ 5/2}$ = 1.3 eV). Subsequent Fe implantation into the Pt_{an} film not much affected the Pt environments, although some minor differences in peak ratios can be noted. Compared with the Pt film, the XPS Pt 4f spectrum of the Pt + Fe sample revealed a strong peak from the $PtTi_x$ compound with a minor contribution from metallic Pt, PtO, and PtO_2 phases. After annealing, the relative intensity of the Pt oxides was observed to increase ($(Pt + Fe)_{an}$ sample).

The fitting of the XPS Ti 2p spectra of the Pt- and Fe-implanted samples both before and after annealing is depicted in Figures 4e−h and S2e−g. The peaks can be fitted by the sum of four components: oxidized titanium [TiO_2 (main component, $BE_{3p\ 3/2}$ = 458.5 ± 0.2 eV, $fwhm_{3p\ 3/2}$ = 1.3 ± 0.1 eV; $BE_{3p\ 1/2}$ = 464.1 ± 0.2 eV, $fwhm_{3p\ 1/2}$ = 1.8 ± 0.1 eV) and Ti_2O_3 ($BE_{3p\ 3/2}$ =

DOI: 10.1021/acsami.9b09649
ACS Appl. Mater. Interfaces 2019, 11, 28699−28719

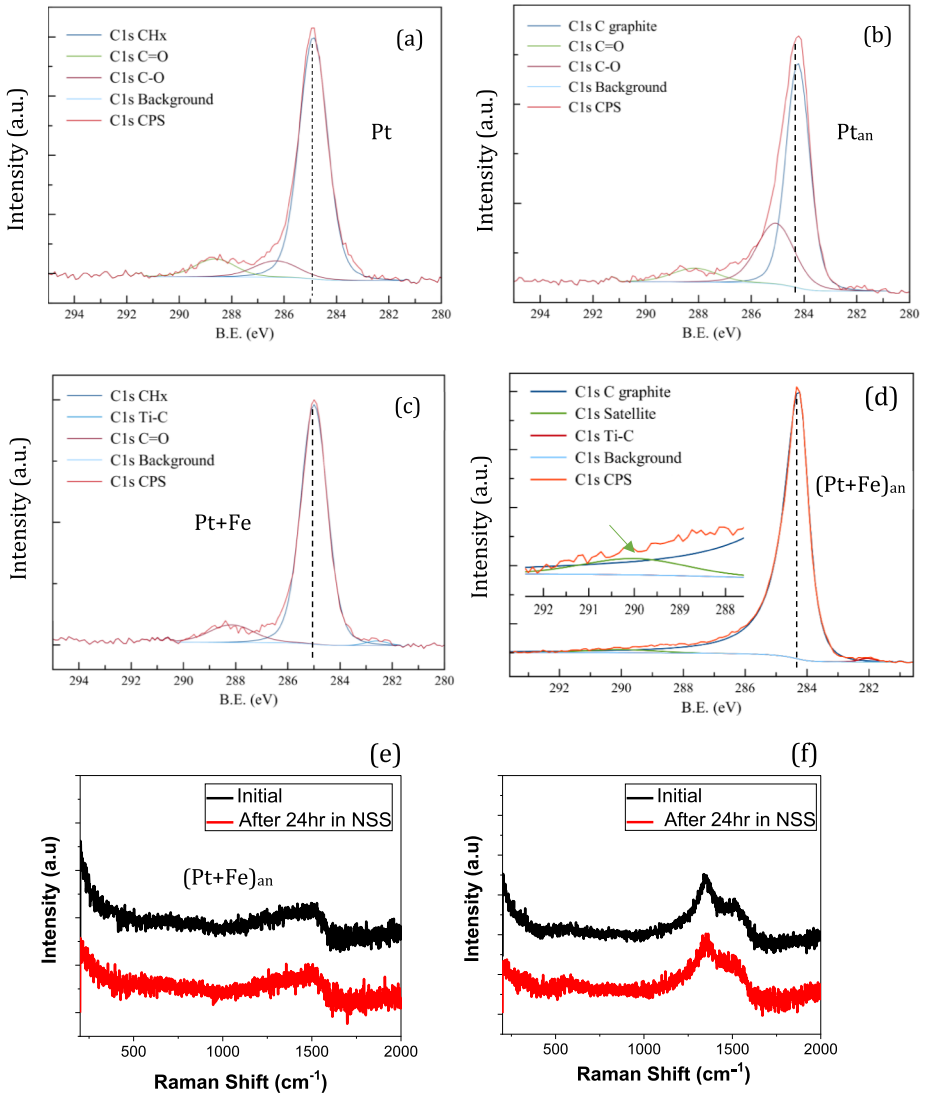

Figure 3. XPS C 1s spectra of Pt, Pt_{an}, Pt + Fe, and $(Pt + Fe)_{an}$ samples and their curve-fitting (a–d). Raman spectra of Pt + Fe (e) and $(Pt + Fe)_{an}$ (f) samples before (black curve) and after exposure in NSS for 24 h (red curve). Arrow (inset in (d)) shows the graphite satellite feature.

457.3 ± 0.2 eV, $fwhm_{3p\ 3/2}$ = 1.5 ± 0.1 eV; $BE_{3p\ 1/2}$ = 462.5 ± 0.2 eV, $fwhm_{3p\ 1/2}$ = 1.8 ± 0.1 eV)] and titanium carbide and nitride [TiC ($BE_{3p\ 3/2}$ = 455.1 ± 0.1 eV, $fwhm_{3p\ 3/2}$ = 1.1 ± 0.1 eV; $BE_{3p\ 1/2}$ = 459.5 ± 0.1 eV, $fwhm_{3p\ 1/2}$ = 1.1 ± 0.1 eV) and TiN ($BE_{3p\ 3/2}$ = 456.0 ± 0.2 eV, $fwhm_{3p\ 3/2}$ = 1.5 ± 0.1 eV; $BE_{3p\ 1/2}$ = 461.0 ± 0.2 eV, $fwhm_{3p\ 1/2}$ = 1.5 ± 0.1 eV)]. Because the TiN and TiC peaks were more pronounced in the XPS spectrum of the Fe-implanted sample, it is reasonable to conclude that it was less oxidized as compared with the Pt-doped counterparts. An interesting observation is that in the presence of Fe or Pt NPs, the surfaces become less oxidized after annealing [the intensities of the TiN and TiC peaks in the XPS Ti2p spectra of the Fe_{an}, Pt_{an}, and $(Pt + Fe)_{an}$ samples were observed to increase]. It is also worth noting that after Fe ion implantation into the Pt_{an} sample, the TiN and TiC peak intensities weakened significantly, hereby indicating that Fe ion implantation promoted surface oxidation.

The XPS O 1s peaks in all samples were fitted using two components: M–O (M = metal) at BE = 530.2 ± 0.2 eV and fwhm = 1.4 ± 0.2 eV and C═O at BE = 532.4 ± 0.3 eV and fwhm = 1.8 ± 0.2 eV (Figure S4). The M–O/C═O peak ratio in different samples was different being minimum for the $(Pt + Fe)_{an}$ sample.

The atomic concentrations of all the elements determined from the curve-fitting of XPS spectra are summarized in Table 2. After ion implantation, the TiCaPCON films contained 11.9 at. % of Fe and 9.2 at. % of Pt. The total content of the implanted elements in the Pt + Fe sample was 11.6 at. %. After annealing, the content of implanted elements significantly decreased to 0.63 at. % (Fe_{an} sample) and 0.3 at. % [$(Pt + Fe)_{an}$ sample]. In contrast, the Pt content increased to 12.7 at. % (Pt_{an} sample). Subsequent Fe ion implantation into the Pt_{an} film led to a decrease in the Pt content to 7.8 at. % because of Pt sputtering by Fe ions and an additional enrichment with Fe (3.4 at. %). It should also be noted that O content markedly decreased in all samples after annealing: from 36.1 (Fe) to 20.8 (Fe_{an}), from 35.5 (Pt) to 16.3 (Pt_{an}), and from 33.2 (Pt + Fe) to 9.1 at. % [$(Pt + Fe)_{an}$].

3.5. XPS (after Immersion in NSS). High-resolution XPS C 1s, N 1s, Pt 4f, Ti 2p, and O 1s spectra are shown in Figures S5–S9. The Ti 2p signals from all samples before and after immersion in NSS were similar. The main feature of the O 1s spectra was the appearance of C–O components. It was also

DOI: 10.1021/acsami.9b09649
ACS Appl. Mater. Interfaces 2019, 11, 28699–28719

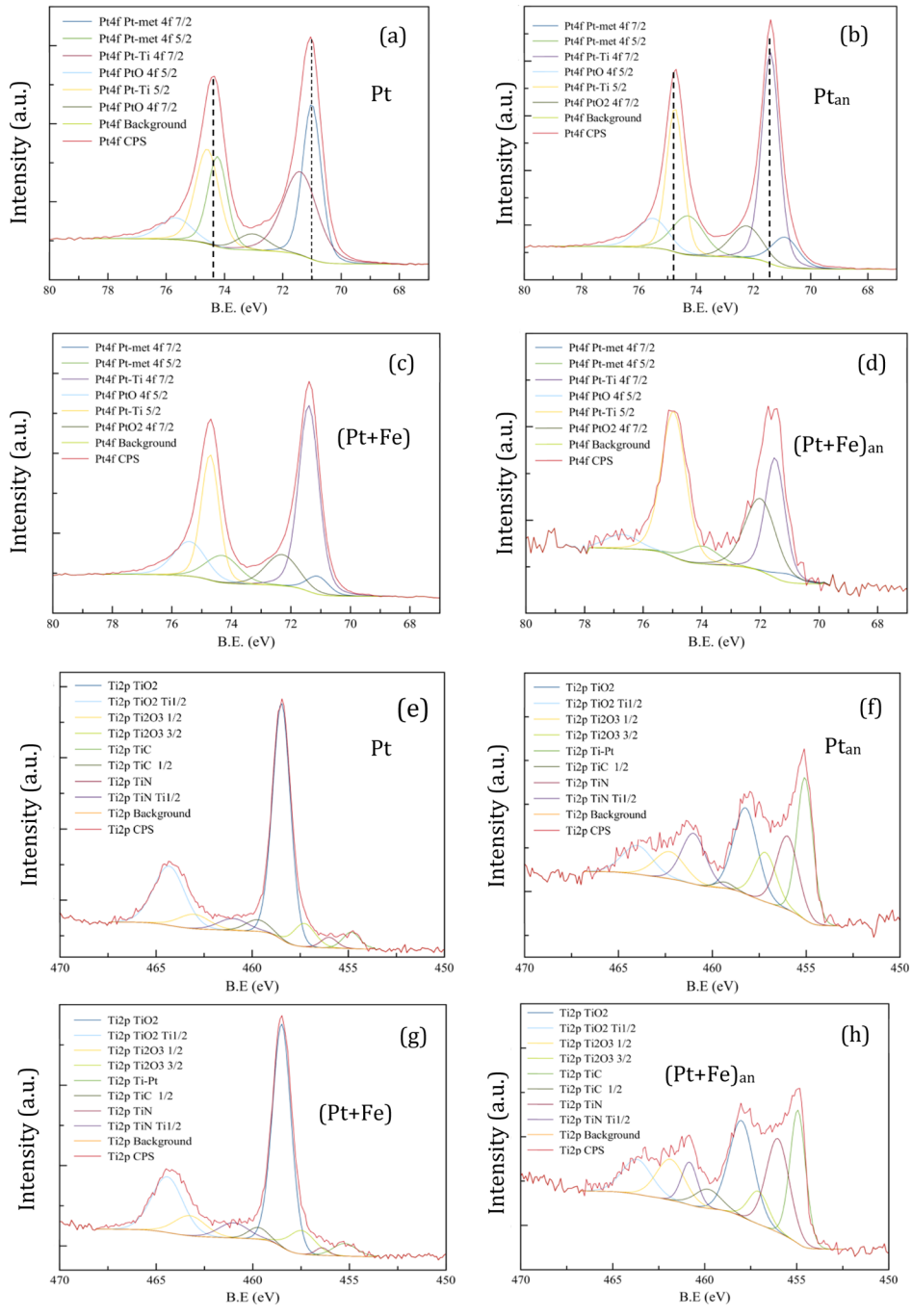

Figure 4. XPS Pt 4f (a–d) and Ti 2p (e–h) spectra of Pt, Pt_{an}, Pt + Fe, and $(Pt + Fe)_{an}$ samples and their curve-fitting.

Table 2. Atomic Concentration of Elements (before Immersion in NSS) According to XPS

sample	concentration, at. %							
	C 1s	Ca 2p	Fe 2p	N 1s	O 1s	P 2p	Pt 4f	Ti 2p
TiCaPCON	48.2	1.5	0.0	9.1	29.0	0.0	0.0	12.2
Fe	46.1	0.0	11.9	2.0	36.1	0.0	0.0	3.9
Pt	39.1	0.2	0.0	1.9	35.5	0.0	9.2	14.1
Pt + Fe	40.3	0.2	4.2	2.2	33.2	0.0	7.5	12.4
Fe_{an}	58.7	0.4	0.6	7.7	20.8	0.0	0.0	11.8
Pt_{an}	58.6	0.4	0.0	4.3	16.3	1.8	12.7	5.9
Pt_{an} + Fe	42.4	0.2	3.4	3.1	31.7	0.0	7.8	11.4
$(Pt + Fe)_{an}$	78.9	0.1	0.0	5.8	9.1	0.0	0.3	5.7

DOI: 10.1021/acsami.9b09649
ACS Appl. Mater. Interfaces 2019, 11, 28699–28719

Table 3. Atomic Concentration of Elements (after Immersion in NSS) According to XPS

sample	concentration, at. %							
	C 1s	Ca 2p	Fe 2p	N 1s	O 1s	P 2p	Pt 4f	Ti 2p
Fe	37.7	0.0	11.9	2.9	40.9	0.0	0.0	6.6
Pt	36.0	0.0	0.0	2.1	37.9	0.0	9.2	14.8
Pt + Fe	35.6	0.0	4.8	2.3	37.2	0.0	7.5	12.6
Fe_{an}	56.6	0.1	2.6	6.9	24.0	0.0	0.0	9.8
Pt_{an}	62.1	0.0	0.0	2.6	17.0	0.9	11.7	5.7
Pt_{an} + Fe	42.1	0.0	4.1	1.8	33.4	0.0	7.6	11.0
$(Pt + Fe)_{an}$	74.6	0.0	1.1	6.3	12.0	0.0	0.3	5.7

noted that during exposure in NSS, the C−N groups completely disappeared in the Fe_{an}, Pt, Pt_{an}, Pt_{an} + Fe, and $(Pt + Fe)_{an}$ samples. The amount of amide N−C═O groups in the Fe-implanted film was observed to also decrease after soaking in NSS. In the Fe-doped samples subjected to annealing [Fe_{an} and $(Pt + Fe)_{an}$], new peaks located at 396.4 eV were observed, which could be attributed to unknown nitride. The C 1s spectra of NP-decorated samples before and after exposure in NSS were more or less the same, although some differences could be noted: (i) additional C−O (Fe_{an} and Pt + Fe) and C−C (Fe) components were observed after immersion in NSS and a-C was substituted by CH_x groups in the Fe_{an} sample. Immersion in NSS also affected the Pt environment: the $PtTi_x/Pt_{met}$ ration increased in the Pt and Pt_{an} + Fe films and the $PtTi_x$/Pt NPs become more oxidized [Pt_{an}, P_{tan} + Fe, $(Pt + Fe)_{an}$].

Comparison of element atomic concentrations before and after immersion in NSS (Tables 2 and 3) revealed that the amount of Ca and P (if detected before exposure in NSS) decreased. This can be explained by a fast Ca and P dissolution (see Section 3.7). It was also noted that the amount of oxygen slightly increased and that of carbon, in samples Fe, Pt, and Pt + Fe, decreased.

Summing up, we note some general regularity: (i) immersion in NSS led to the disappearance of C−N components and appearance of C−O groups, (ii) Pt and $PtTi_x$ NPs had a tendency to oxidation in NSS where the Pt NPs oxidize faster. In the Fe-doped samples, the surface chemistry changed more significantly during exposure in NSS: additional unknown nitride was observed [Fe_{an}, Pt_{an} + Fe, and $(Pt + Fe)_{an}$] and a-C transformed into CH_x groups.

3.6. Wettability. The bacterial adhesion can be controlled via surface wettability. The film wettability was evaluated after 2 weeks of sample storage in plastic bags (Table 4). The films with NPs on their surface exhibited contact angles ranging from 81° to 90°, indicating that all the surfaces were slightly hydrophilic. The TiCaPCON film without NPs showed a water contact angle approximately 73°. The water drops were observed to spread over the surface over time. As a result, the contact angle values of NP-decorated samples decreased to 57−70° (after 5 min) and further to 23−32° (after 10 min).

Table 4. Water Contact Angles

samples	water contact angle, °		
	0 min	5 min	10 min
TiCaPCON	74 ± 2	44 ± 1	13 ± 1
Pt	97 ± 2	73 ± 1	23 ± 2
Pt_{an}	90 ± 1	62 ± 2	19 ± 1
Fe	90 ± 1	61 ± 2	15 ± 2
Fe_{an}	82 ± 2	54 ± 1	16 ± 1
Pt + Fe	91 ± 2	70 ± 1	28 ± 1
$(Pt + Fe)_{an}$	94 ± 1	71 ± 1	26 ± 2
Pt_{an} + Fe	89 ± 3	70 ± 2	29 ± 2

3.7. Ion Release. Figure 5a illustrates the amount of Pt ions leaching out from the Pt-doped TiCaPCON films into NSS over time. Pt NPs did not dissolve; therefore, the concentration of Pt ions was below 1.5 ppb after 72 h. The situation has changed dramatically after the Fe ion implantation (Pt + Fe sample). The concentration of Pt ions rapidly increased to 18 ppb within 6 h and then Pt ion release eventually stopped. The time-dependent release of Pt ions in the presence of Fe can be explained as follows.[22] After Fe ion implantation into the Pt film, Fe ions were embedded into the Pt NPs already located on the film surface. In the NSS, Fe ions rapidly dissolved from the surface of Pt NPs dragging along some Pt ions. Once Fe ions were released, the remaining large-surface-area Pt matrix potentially became highly

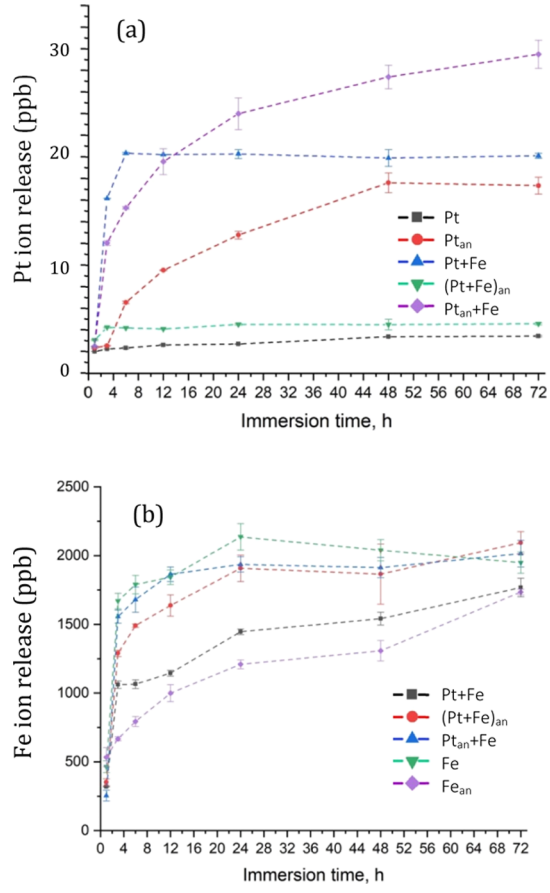

Figure 5. Concentrations of Pt (a) and Fe (b) ions released into NSS over time, as measured by ICP-MS.

DOI: 10.1021/acsami.9b09649
ACS Appl. Mater. Interfaces 2019, 11, 28699−28719

defective and prone to accelerated dissolution. These explain Pt ion release over the first 6 h. When Pt NPs became free from Fe atoms, their dissolution almost completely terminated. After annealing of the Pt + Fe sample [$(Pt + Fe)_{an}$], the Pt ion release was observed to be low. The Pt ion concentration slightly increased to 2 ppb during 3 h and did not change further. According to XPS data, after annealing, Pt was bound to Ti and no Fe was detected (Table 2). This well explains why the time-dependent release of Pt ions in the $(Pt + Fe)_{an}$ sample was similar to that in the Pt counterpart. In the Pt_{an} and Pt_{an} + Fe samples, the concentration of Pt ions gradually increased with time reaching 14 (Pt_{an}) and 27 ppb (Pt_{an} + Fe) after 72 h. Apparently, the potential difference between the NPs and the surrounding matrix has become smaller because of Pt → $PtTi_x$ transformation, Pt oxidation, and TiO_2 reduction, thereby allowing Pt ion release. The presence of Fe accelerated the Pt ion leaching out of the surface because of dragging effect as described above (Pt_{an} + Fe).

Iron quickly dissolved in NSS, and its concentration in the Fe sample reached 1750 ppb already after 3 h (Figure 5b). In the annealed film (Fe_{an}), the Fe ion release significantly slowed down because of Fe NP oxidation; after 3 h, the Fe ion concentration was only about 500 ppb. The Fe content in the Pt-doped samples was lower compared with their Pt-free counterparts because of the difference in the ion implantation regimes: 30 kV, 60 min (Fe); and 25 kV, 15 min (Pt + Fe and Pt_{an} + Fe). Thus, after 3 h, only 1100 ppb was leached out of the Pt + Fe film surface compared with 1750 ppb in the Fe sample. During annealing, the Pt and Fe atoms completely separated from the Fe-implanted Pt NPs and formed two isolated NPs: Pt/PtTi (cathodes) and Fe (anodes). In the presence of active cathodes, the concentration of Fe ions in the NSS significantly increased [$(Pt + Fe)_{an}$]. The Pt_{an} + Fe sample also exhibited a high Fe ion release. After annealing, the number of Pt NPs significantly increased (Figure 1b) and a larger amount of Fe was implanted into the Pt NPs. This increased the number of cathode−anode (Pt + Fe) pars, which accelerated Fe ion leaching from the surface into NSS.

Summarizing the results described above, we can conclude that three main factors, namely, the existence of active cathodes, the potential differences between NPs and the surrounding matrix, and "dragging" effect, had a significant impact on the Pt and Fe ion release.

Figure S10 depicts the concentration of Ca, P, and Ti ions after sample exposure in NSS for various times. The concentration of Ca ions rapidly increased within 12 h and then remained approximately at the same level in the range of 30−40 ppm. All films demonstrated a high P ion release within first 3 h, followed by a slower ion leaching over 48 h. The average amount of P ions was found to be 2−3.5 ppm (3 h) and 3−6.5 ppm (72 h). The concentration of Ti ions reached 200−280 ppb already after 1 h and then the Ti dissolution significantly slowed down. After 48 h, the Ti ion release accelerated again.

3.8. Specular Reflectance IR Spectroscopy. In order to understand the film reflectivity under UV and visible light, the samples were analyzed by SR-IR. Figure S11 compares the SR-IR spectra of the NP-free TiCaPCON film and those decorated with metallic NPs recorded at an incidence angle of 30, 40, 50, and 60 degree. The specular reflectance was below 40% in the range of 200−1000 nm. All spectra had a similar appearance in the measured wavenumber range. The wavelength at a minimum (450 and 600−700 nm) and maximum (580 nm) reflectance is unaffected by the surface chemistry. At an incidence angle of 60 degree, Fe_{an} and Pt_{an} samples show minimum reflection in the UV and visible light range, respectively. In contrast, a maximum reflection at 580 nm was observed for Fe and Pt samples.

3.9. Formation of ROS. ROS concentration was measured after exposure to various irradiation conditions: after UV and visible light irradiations for 30 min and 8 h, respectively, and after storage in the dark for 8 h. Figure 6 shows the concentrations of ROS after sample immersion in NSS for 1, 3, 12, and 24 h. The TiCaPCON film without NPs on its surface generated ROS only after UV exposure (Figure 6a). The maximum ROS concentration was observed after 3 h (450 nmol/cm^2), and longer exposure to UV led to the decreased ROS concentration of 190 nmol/cm^2 (after 12 h). When excited under UV irradiation, the Pt- and Fe-doped samples showed the maximum ROS concentrations after immersion in NSS for 3−12 h: 720 (Pt), 1700 (Pt_{an}), 1310 (Fe_{an}), 2970 (Pt + Fe), 1970 (Pt_{an} + Fe), and 1180 nmol/cm^2 [$(Pt + Fe)_{an}$]. After 24 h, the ROS concentration was observed to be significantly decreased to 300 (Pt), 730 (Pt_{an}), 900 (Fe_{an}), 300 (Pt + Fe), 310 (Pt_{an} + Fe), and 170 nmol/cm^2 [$(Pt + Fe)_{an}$]. In the case of exposure to visible light (Figure 6b), the maximum ROS concentration was observed to be approximately 2−3 times lower: 385 (Pt), 620 (Pt_{an}), 450 (Fe_{an}), 840 (Pt + Fe), 870 (Pt_{an} + Fe), and 460 nmol/cm^2 [$(Pt + Fe)_{an}$]. Under both UV and visible light exposure conditions, the ROS concentration is observed to be higher for the Pt + Fe and Pt_{an} + Fe films. These two samples also

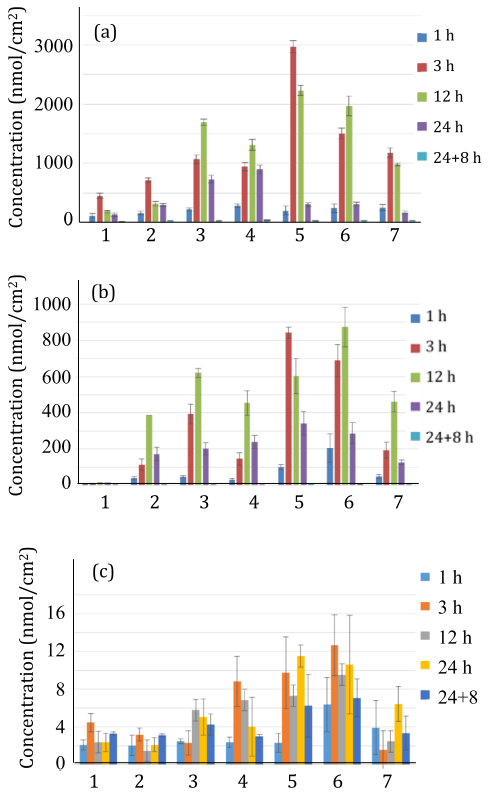

Figure 6. Concentration of ROS generated in NSS after UV irradiation for 1 h (a), during exposure to artificial light (b) and dark (c), as determined by fluorescence spectrophotometry. 1—TiCaPCON, 2—Pt, 3—Pt_{an}, 4—Fe_{an}, 5—Pt + Fe, 6—Pt_{an} + Fe, and 7—$(Pt + Fe)_{an}$. 24 + 8 h denotes samples which were preliminarily kept in NSS for 24 h, then the solution was replaced with a new one, and finally the ROS concentration was measured after 8 h.

DOI: 10.1021/acsami.9b09649
ACS Appl. Mater. Interfaces 2019, 11, 28699−28719

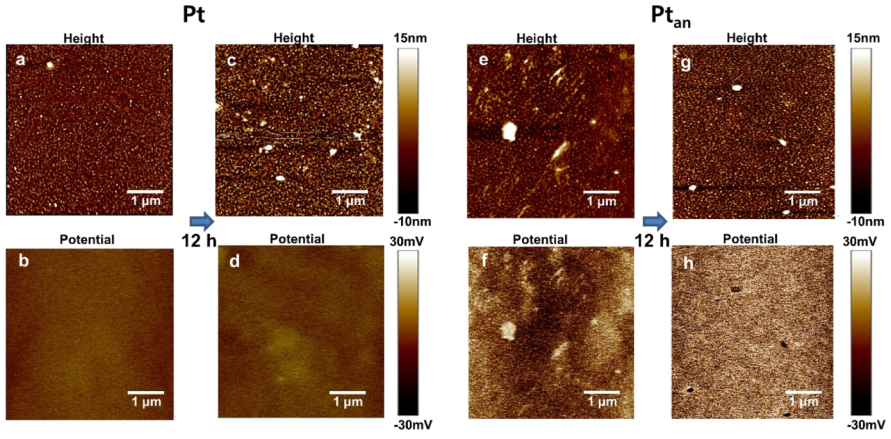

Figure 7. AFM height profile (a,c,e,g) and corresponding Kelvin probe force microscopy (b,d,f,h) images of the samples with Pt and Pt_{an} NPs on their surface. The measurements were carried out before (a,b,e,f) and after 12 h (c,d,g,h) exposure to the normal saline (0.9 wt % NaCl) solution.

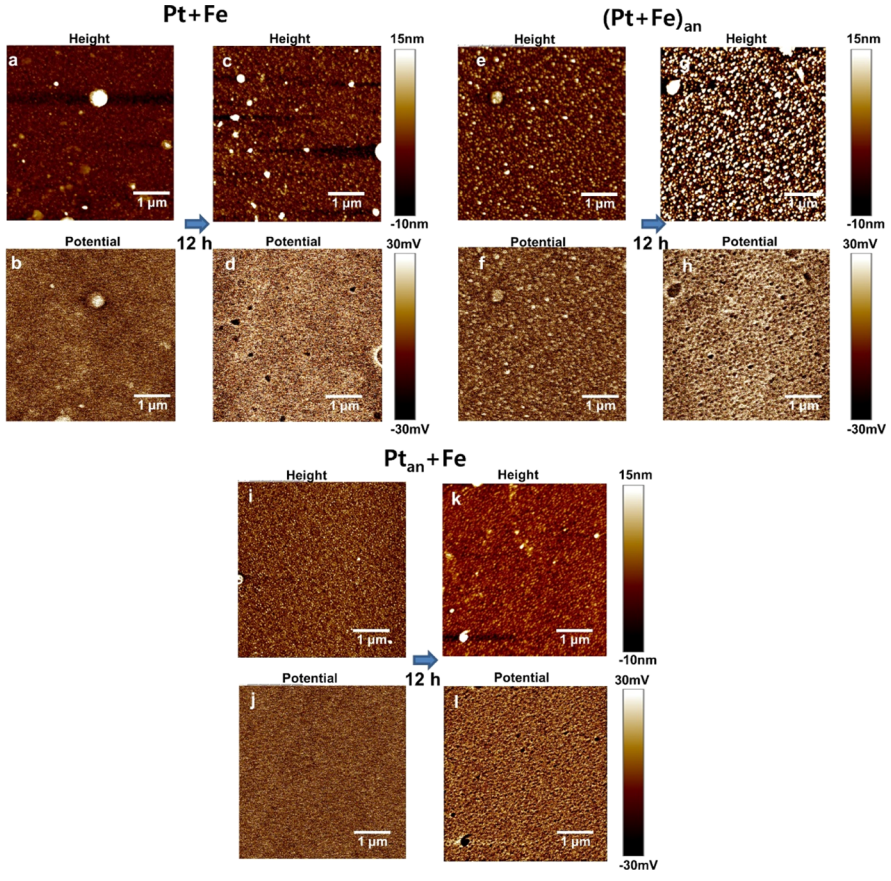

Figure 8. AFM height profile (a,c,e,g,i,k) and corresponding Kelvin probe force microscopy (b,d,f,h,j,l) images of the samples with Pt + Fe, $(Pt + Fe)_{an}$, and Pt_{an} + Fe NPs on their surface. The measurements were carried out before (a,b,e,f,i,j) and after 12 h (c,d,g,h,k,l) exposure to the normal saline (0.9 wt % Na Cl) solution.

generated a maximum amount of ROS in the dark (Figure 6c), but ROS concentration was significantly lower (<13 nmol/cm^2).

The ROS concentration depends on two competitive processes: ROS formation and recombination. Figure S12 shows the concentrations of ROS in aliquots collected at intervals of 12 h and stored for 66 and 54 h, respectively. Comparison of the results presented in Figures 6 and S12 indicates that the ROS concentration in aliquots (without samples) decreases with time at a rate of 1.3−7.8 nmol/cm^2 per h.

3.10. Atomic Force Microscopy and Kelvin Probe Force Microscopy. Figure 7 shows the AFM height profiles and the corresponding Kelvin probe force microscopy images of the TiCaPCON films with Pt and Pt_{an} NPs on their surfaces. All measurements were carried out before and after 12 h exposure in the NSS. The AFM images of Pt-implanted samples (Figure 7a,c) revealed that the sample surfaces are heavily populated with Pt NPs, about 25 nm in size, similar to those observed in the SEM image presented in Figure 1a. Several large Pt particles (crystallized droplets), 150−200 nm in size, were also observed.

DOI: 10.1021/acsami.9b09649
ACS Appl. Mater. Interfaces 2019, 11, 28699−28719

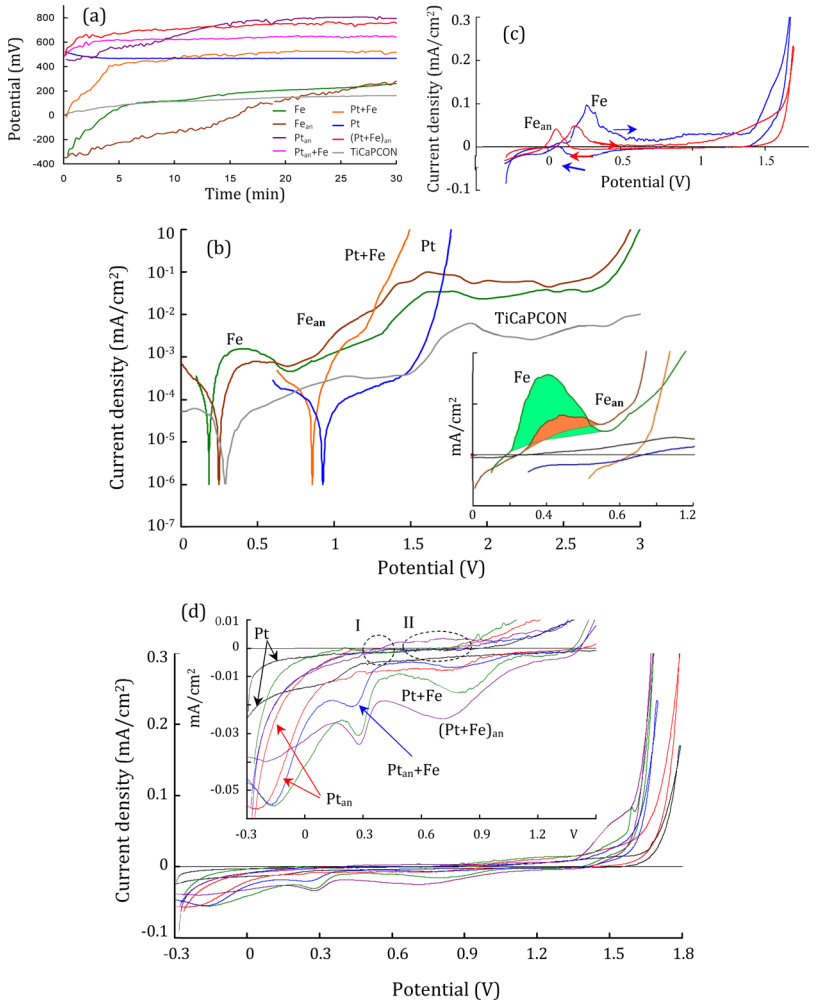

Figure 9. The variation of free corrosion potential over time (a). Typical APP curves obtained with the sweep rate of 3 mV/s (b). Inset shows initial parts of the polarized curves. The areas of current density peaks corresponding to Fe NP oxidation are shown in color. Typical APP curves of the Fe and Fe_{an} samples (the rate of the potential sweep is 10 mV/s) (c). Typical APP curves of the Pt, Pt + Fe, Pt_{an} + Fe, and $(Pt + Fe)_{an}$ films, obtained at a potential sweep rate of 10 mV/s (d). Inset indicates the ranges of the potentials of the zero current densities for $(Pt + Fe)_{an}$ film (I), all other films (II), and the current density peaks of the Fe-doped films on the curves with the reverse potential sweep (III).

Both types of Pt NPs were not observed in the corresponding Kelvin images, and there is no clear potential difference between the Pt NPs and the surrounding TiCaPCON matrix. The situation was changed after the sample annealing, where the images reveal a clear correlation between the location of Pt_{an} NPs and the Kelvin map (Figure 7e–h). The Pt_{an} NPs had a more positive potential than the surrounding matrix, the difference being about 15–30 mV (Figure 7f). It is important to note that after exposure in NSS for 12 h, the potential difference between the Pt_{an} NPs and the surrounding matrix was changed; the Pt_{an} NPs become negatively charged with respect to the matrix (Figure 7h).

The AFM and Kelvin probe images of Fe-implanted samples were less informative. Similar to the SEM image presented in Figure 1c, the Fe NPs were not observed using AFM, except several large Fe droplets (Figure S13). After annealing, the small and large Fe_{an} NPs become better visible (Figure S11e), which is in good agreement with the corresponding SEM image (Figure 1d). In the Kelvin probe images, Fe droplets and some Fe_{an} NPs (Figure S13b,f) with more positive potentials can be distinguished. Note that no potential differences between Fe/Fe_{an} NPs and surrounding matrix were observed in the corresponding Kelvin probe images after exposure in NSS (Figure S13d,h).

AFM and corresponding Kelvin probe images of the Pt + Fe, $(Pt + Fe)_{an}$, and Pt_{an} + Fe films are presented in Figure 8. In all cases, there is a good correlation between topography and potential maps. Clear AFM and Kelvin probe images with NP resolutions were obtained for the $(Pt + Fe)_{an}$ sample (Figure 8e–h). Immediately after immersion in the NSS, the NPs were positively charged relative to the matrix (with approximately 30 mV potential difference). However, after exposure in NSS for 12 h, the NPs become more negatively charged, and the potential difference was as high as 40–50 mV. Thus, NPs exhibit high potential differences with respect to the matrix, thereby indicating that microgalvanic couples are formed when both electrodes (NPs and matrix) are in conducting state. A similar change of NP charge during exposure in NSS was observed for the Pt + Fe and Pt_{an} + Fe films.

3.11. Electrochemical Behavior. The following experiments were carried out in conditions providing the maximum protection of NPs from their dissolving. For this, the initial potential for recording polarized curves for all samples was chosen at −0.3 V. The rate of the potential sweep was increased

DOI: 10.1021/acsami.9b09649
ACS Appl. Mater. Interfaces 2019, 11, 28699–28719

to 10 mV/s, which also promotes the preservation of the Fe NPs before achieving typical potentials of NP dissolution. In addition, the polarization curves with the reverse potential sweeps were recorded from the values of maximum anodic potential sweeps (+1.7 V) to the initial potential (−0.3 V). This helps to identify the contribution of a passive oxide layer, formed on the surface with the TiCaPCON film, to general kinetics of the NP dissolution.

The change in the free corrosion potential provides information about dissolving less stable elements of the film and the surface passivation, linked to the formation of oxide layers. The variation of the free corrosion potential of the film with time is shown in Figure 9a. It is clear that within 30 min, the potential of the TiCaPCON film shifts from the initial value of 30 mV to +150 mV, which is probably related to the fast dissolving of Ca and P (in agreement with ion release data) and forming a passive Ti oxide layer. The Fe implantation into the TiCaPCON film leads to the displacement of the initial potential to a more negative value of −320 mV, which is close to the pure Fe potential in the environment. During the first 10 min, the potential shifts to the +110 mV. Following this, during the last 20 min of the measurements, it slowly raises to +250 mV, appearing to be 100 mV more positive than the potential obtained for the Fe-free film. A similar dependence was obtained for the Fe_{an} sample; however, the potential increase was more uniform over time. It could be assumed that this is connected to the oxidation of the Fe NPs because Fe oxides and hydroxides have more positive potentials than these of Ti oxides.

For the pure metallic Pt, the equilibrium potential is +990 mV. The potential for the Pt film stabilizes quickly at the level of +450 mV. This corresponds to an intermediate value between the Pt NP potential and the Ti oxide potential. After the annealing, the size and the relative area of the NPs on the surface had increased. As a result, the potential of the Pt_{an} coating shifted to a more positive value of +800 mV.

The equilibrated potentials of the Pt, $(Pt + Fe)_{an}$, and Pt_{an} + Fe films are in the range from the +550 to +750 mV, and generally, they are controlled by the Pt NPs. It could be assumed that the Fe NPs, which are subjected to impose potentials from the Pt NPs, dissolve rapidly and the observed difference between behaviors of the individual curves shown in Figure 9a is linked to the size, amount, and the chemical state of the Pt NPs, as well as their activity change over the time.

In Figure 9b, the typical anodic potentiodynamic polarization (APP) curves of films are shown. When the polarization values are low, the TiCaPCON film is in a stable passive state condition. At 1.5 V, an activation peak is observed, which is linked to two competitive processes: Ti dissolving and isolation of film surface with a growing passive layer.

APP curves of the Pt films show typical behavior for pure metallic Pt. The observed growth of the current density at the potential of 1.5 V and the lack of passivation are linked to water electrolysis and the release of O_2. The Fe implantation in the Pt film leads to the acceleration of anodic processes. This could be linked to the change of the Pt sample chemical state on the surface after the Fe implantation and dissolution of the Fe ions, dragging along some Pt ions.

For the Fe sample at +0.3 V potential, there is the typical peak of Fe current density that evidences its oxidation. After annealing (Fe_{an} sample), the area of the Fe current density peak is considerably decreasing (Figure 9b, inset). This represents that there is a much fewer amount of the metallic (unoxidized) Fe in the Fe_{an} film than in the Fe counterpart. After Fe dissolving, the behavior of the APP curves of Fe and Fe_{an} films repeats the behavior of the current density on the potential observed for the TiCaPCON sample. However, the anodic current densities for samples with Fe are higher. This is linked to the decrease in the protective properties of the Ti oxide layer on the film surface in the presence of the Fe oxidation products.

Figure 9c shows the APP curves of the films, with Fe, which were obtained with the increased rate of the potential sweep. In contrast with the APP curves, as shown in Figure 9b, the following differences could be noted. Zero current potential of the Fe and Fe_{an} films shifted to a negative value (the line of the current density crosses the abscissa axis at negative potentials) that indicates a larger amount of preserved Fe NPs. For both films, the typical peaks of the current density are observed at potentials in the range of 0.3 to 0.4 V, which is probably linked to the Fe NP oxidation. The current density curves, obtained with reverse potential sweeps from the maximum anodic potential of +1.5 to +0.5 V, show very low values of current densities, which is related to a high quality of passive layer formed on the areas of the TiCaPCON films, which are not occupied by Fe NPs. It is important to note that in the potential range of +0.5 to −0.2 V, the current density curves of the Fe and Fe_{an} films differ considerably. For the Fe-doped TiCaPCON sample, there is a current density peak with negative polarity at the reverse potential sweep, which is probably linked to a partial reduction of the iron oxide Fe_2O_3 to an oxide with a reduced degree of oxidation FeO_x. In the Fe_{an} sample, this current density peak has a positive polarity and is shifted to more negative potential values as compared to the peak, obtained during the direct potential sweep. Such peak displacements can be related to the higher rate of the potential sweeps.

Figure 9d shows the APP curves of the Pt, Pt + Fe, Pt_{an} + Fe, and $(Pt + Fe)_{an}$ films that were obtained with the rate of the potential sweeps of 10 mV/s. The initial current density curves obtained in the anodic sweep direction are very similar for all Pt-containing films. The zero current potentials for all the studied samples, with an exception of $(Pt + Fe)_{an}$, are in the range from +0.5 to +0.9 V (Figure 9d, inset, area II), which is linked to the presence of the Pt NPs. In the case of $(Pt + Fe)_{an}$ film, the zero running potential is +0.35 V (Figure 9d,inset, area I).

When the potentials are more positive than +1.5 V (as well as on the curves obtained at the lower sweep rate), there is a characteristic steep growth of the current density for all Pt-doped films, linked to the electrochemical water dissociation and oxygen release. This is also confirmed by the cathode curve of the reverse potential sweep, which in this range practically repeats the anodic curve (lack of the hysteresis). Low current density at potentials less than +1.5 V corresponds to the passive state of TiCaPCON film. At the negative potential values, the cathodic current density of the Pt-doped films rises because of the hydrogen release (the potentials are referenced to the hydrogen electrode, for which zero corresponds to the hydrogen reduction). On the curves of the reverse sweep for the Fe-doped films, there are negative peaks of the current density in the potential range from +0.3 to +0.2 V (Figure 9d, inset, area III). This confirms the reduction of Fe_2O_3 to Fe oxides with a lower oxidation degree. This result is important for the understanding of the potential distributions on sample surfaces after holding in a salt solution. Probably, only part of Fe NPs dissolves and leaches into the solution in the form of ions. Another part of Fe NPs is oxidized to the Fe oxide and remains on the film surface even after significant anodic polarization. The electrochemical potential of these NPs corresponds to the value of +0.3 V, which

DOI: 10.1021/acsami.9b09649
ACS Appl. Mater. Interfaces 2019, 11, 28699−28719

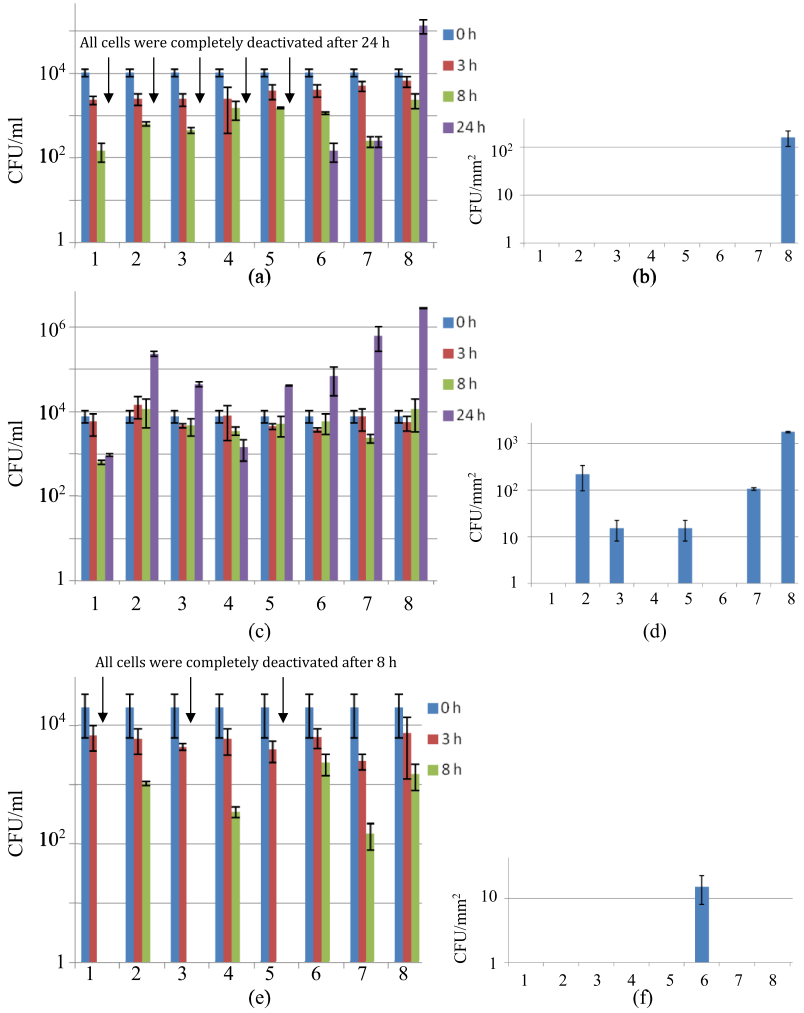

Figure 10. Antibacterial activity of samples against the *E. coli* U20 (a), *E. coli* K261 (c), and *S. aureus* 839 (e) strains and biofilm formation on the sample surfaces (b,d,f). 1—Fe, 2—Pt, 3—Pt + Fe, 4—Pt_{an} + Fe, 5—Fe_{an}, 6—Pt_{an}, 7—$(Pt + Fe)_{an}$, and 8—control (TiCaPCON film without NPs on the surface).

is more positive than that of the TiCaPCON film potential of +0.15 V.

3.12. Antibacterial Activity. The sample antibacterial activities against planktonic antibiotic-sensitive *E. coli* U20 strains were studied first (Figure 10a). The TiCaPCON film without NPs on its surface was used as a control. The Fe, Pt, Pt + Fe, Pt_{an} + Fe, and Fe_{an} samples completely eliminated the cells after 24 h. In the case of Pt_{an} and $(Pt + Fe)_{an}$ films, the CFU/mL values were observed to decrease by almost 2 orders of magnitude (the antibacterial effect was 97−98%). The Fe, Pt, and (Pt + Fe) samples demonstrated a pronounced antibacterial effect (CFU/mL values decreased by 2−3 orders of magnitude) already after 8 h. The additional independent antibacterial test was carried out with newly deposited Pt_{an}, $(Pt + Fe)_{an}$, Fe_{an}, Pt, and Pt + Fe films (Figure S14). The results were highly reproducible: all test samples demonstrated a high antibacterial effect (CFU/mL values decreased by three-four orders of magnitude) already after 8 h. The number of cells on the surface of the control sample (TiCaPCON film without NPs in its surface) was almost constant. It is well known that bacteria prefer to colonize a solid substrate rather than dwell in a planktonic state.[48] In order to estimate the contribution of NPs in the early stage of biofilm formation, the coupon method was used. The obtained results show that, unlike the control sample without NPs, there is no biofilm formation on the NPs containing surfaces (Figure 10b). Thus, our data clearly demonstrate that all NP-decorated samples possess a strong antibacterial effect against *E. coli* U20 bacteria and inhibit the early stage of biofilm formation.

The antibacterial test results against antibiotic-resistant *E. coli* K261 cells are presented in Figure 10c. Only the Fe and Pt_{an} + Fe samples showed a noticeable antibacterial activity after 8 (Fe) and 24 h (Pt_{an} + Fe); the antibacterial effect was 91 and 80%, respectively (the CFU/mL values decreased by 1 order of magnitude). The Fe, Pt_{an} + Fe, and Pt_{an} films completely suppressed biofilm growth on their surfaces. Note that on the surfaces of Pt, Pt + Fe, Fe_{an}, and $(Pt + Fe)_{an}$ films, the density of CFUs was also lower compared with control (Figure 10d).

The Fe, Fe_{an}, and Pt−Fe samples exhibited a high antibacterial activity against *S. aureus* 839 strains; all cells were completely deactivated after 8 h (Figure 10e). The number of CFU in the presence of Pt_{an} + Fe and $(Pt + Fe)_{an}$ samples has also decreased after immersion in the *S. aureus* bacterial suspension for 8 h. Note that *S. aureus* strains usually do not survive for 24 h even in a nontoxic control sample.[49,50] All samples including control prevented biofilm formation on their surfaces (Figure 10f).

Four samples, Fe, Pt_{an}, Pt_{an} + Fe, and $(Pt + Fe)_{an}$ were selected for more extensive antibacterial testing using eight types of

DOI: 10.1021/acsami.9b09649
ACS Appl. Mater. Interfaces 2019, 11, 28699−28719

bacteria (*E. coli* K261, *K. pneumoniae* B1079k/17-3, *A. baumannii* B1280A/17, *S. aureus* no. 839, *S. epidermidis* i5189-1, *E. faecium* Ya-235: VanA, *E. faecium* I-237: VanA, and *E. coli* U20). The Pt_{an} sample was only effective against *S. aureus* and *E. coli* U20 strains (Figure 11a). Unlike the other test (Figure 10a),

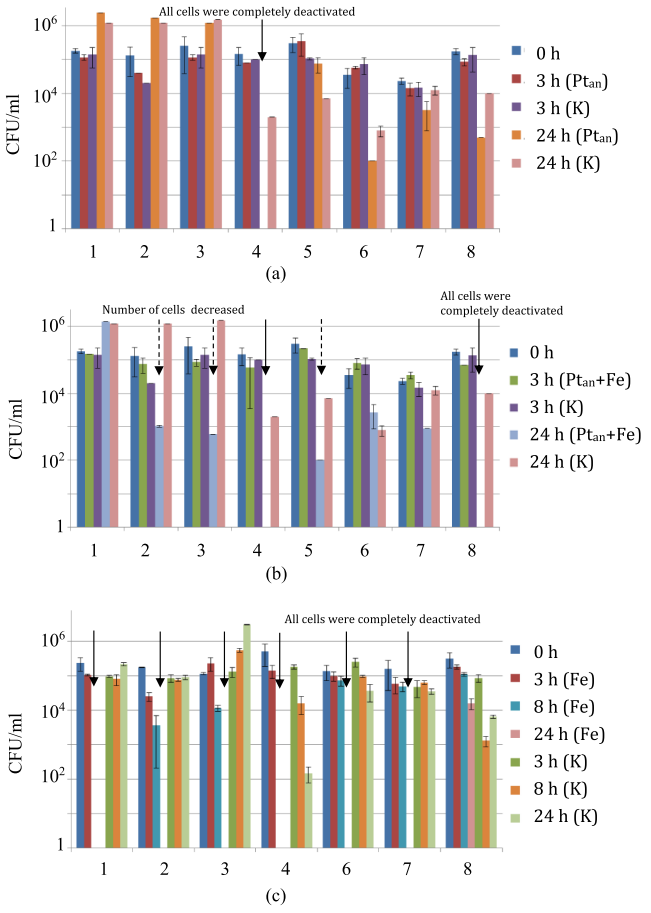

Figure 11. Antibacterial activity of Pt_{an} (a), Pt_{an} + Fe (b), and Fe (c) samples against different bacterial strains. 1—*E. coli* K261, 2—*K. pneumoniae* B1079k/17-3, 3—*A. baumannii* B1280A/17, 4—*S. aureus* no. 839, 5—*S. epidermidis* i5189-1, 6—*E. faecium* Ya-235: VanA, 7—*E. faecium* I-237: VanA, and 8—*E. coli* U20. K—control (TiCaPCON film without NPs on their surface). Test (c) with *S. epidermidis* i5189-1 was not successful.

the lack of antibacterial effect on *E. coli* K262 strain can be explained by higher initial bacteria concentration (10^5 instead of 10^4 CFU/mL). After 24 h, the $(Pt + Fe)_{an}$ films inhibited the growth of *E. faecium* Ya-235: VanA (55%) and *E. faecium* I-237: VanA (one order decrease in CFU/mL, 92%) bacterial colonies but were not effective toward other bacterial strains (Figure S15). Besides *E. coli* U20, *E. coli* K261, and *S. aureus* no. 839, the Pt_{an} + Fe sample exhibited a high antibacterial efficacy against four more cell types (Figure 11b), namely, *K. pneumoniae* B1079k/17-3 (2 orders decrease in CFU/mL, 99%), *A. baumannii* B1280A/17 (2 orders decrease in CFU/mL, 99%), *S. epidermidis* i5189-1 (3 orders decrease in CFU/mL, 99.9%), and *E. faecium* I-237: VanA (1 order decrease in CFU/mL, 90%). The Fe samples exhibited the best antibacterial characteristics in comparison with other tested samples: it completely inactivated the *E. faecium* Ya-235: VanA strains and was more efficient toward *E. faecium* I-237: VanA and antibiotic-resistant *E. coli* K261 bacteria (Figure 11c). For the sake of completeness, we note that the results of antibacterial tests performed at different times may differ slightly from each other (Table 9).

3.13. Influence of Pt- and Fe-Decorated TiCaPCON Films on Immune Cells. Implant-associated infection is a complex combination of pathogens, implant, and the immune system. Therefore, there is a need for simultaneous comprehensive study of the bactericidal and immunomodulatory activity of NP-containing surfaces. NPs interact with the immune system and modulate its function.[51] Samples with Pt and Fe NPs were selected for cytotoxicity tests. Table 5 compares the percentage of dead mononuclear cells in cell cultures with and without test samples. The Pt- and Fe-implanted films did not affect the viability of lymphocytes after 1 and 2 days of incubation. In the case of the Pt film, the number of dead mononuclear cells slightly increased after 7 days.

Table 5. Percentage of Dead Mononuclear cells in Cell Cultures

sample	incubation time, days		
	1	2	7
cultural medium (control)	0.2	1.0	1.5
cultural medium + TiCaPCON−Fe	5.3	3.4	5.8
cultural medium + TiCaPCON−Pt	4.9	5.6	8.0

The Pt- and Fe-doped samples did not affect the proliferation activity of lymphocytes (Table 6). A slight decrease of the proliferation activity of lymphocytes induced by Con A mitogen was observed, but the difference with control was not statistically significant.

Table 6. Proliferation Activity of Lymphocytes

sample	number of proliferating cells, %	
	medium	medium + Con A
cultural medium (control)	0.4	71.6
cultural medium + TiCaPCON−Fe	1.1	61.8
cultural medium + TiCaPCON−Pt	0.9	67.2

After 48 h of incubation, the percentage of CD3+ T-lymphocytes and CD19+ B- lymphocytes in the Pt- and Fe-contained samples was 83.4 ± 0.7 and 8.1 ± 0.6%, respectively, and did not differ from the control (results not shown). One of the indicators reflecting cell activation is the increased expression of activation markers, in particular, the CD69 early activation marker and the CD25 (subunit of the alpha receptor IL-2). A comparative analysis of the number of B-lymphocytes carrying a CD69 marker on their surface showed that in the presence of Fe and Pt NPs, the percentage of CD19+CD69+ cells increases more than 2 and 3 times, respectively (Table 7). In the case of the Pt- and Fe-implanted samples, the expression of the CD25 molecule on the surface of B-lymphocytes was also increased. In the presence of NPs, an enhancement of the CD69 early activation marker on the T-lymphocyte surfaces should be noted. The number of T-lymphocytes carrying a molecule on the CD25 surface was not significantly different between the samples.

The results indicated that the Pt- and Fe-doped TiCaPCON films do not have a pronounced toxic effect on cells; the percentage of dead cells after 7 days was less than 6−8%. NPs did not affect the proliferative activity of lymphocytes, that is, nonspecific activation of cells in the presence of NPs did not

DOI: 10.1021/acsami.9b09649
ACS Appl. Mater. Interfaces 2019, 11, 28699−28719

Table 7. Changes in the Expression Level of CD69 and CD25 Activation Markers on the Surface of T- and B-Lymphocytes

sample	lymphocyte subpopulation, %			
	CD19+CD69+	CD19+CD25+	CD3+CD69+	CD3+CD25+
RPMI	9.7	23.2	0.6	4.8
TiCaPCON−Fe	23	29.7	3.8	4.9
TiCaPCON−Pt	31.4	34.1	7.1	5.3

occur, and NPs had no any notable effect on the ability of lymphocytes to activate in response to a mitogen. Nevertheless, some lymphocyte response to NPs was observed as evidenced by the increased expression of activation markers on the surface of both B- and T-lymphocytes.

4. DISCUSSION

4.1. Phase Transformations during Annealing. The XPS results described above clearly demonstrated that the surface chemistry is undergoing significant changes during metal ion implantation and subsequent annealing. On summarizing XPS data, several important observations can be mentioned.

(i) Pt interacts with Ti to form intermetallic $PtTi_x$ compounds both during Pt ion implantation and subsequent heat treatment. This was well documented for all Pt-containing samples using XPS. The amount of $PtTi_x$ intermetallic phase significantly increased after annealing.

(ii) Annealing in vacuum led to film graphitization [Pt_{an}, Fe_{an}, and $(Pt + Fe)_{an}$ samples].

(iii) In the presence of Fe or Pt NPs, the sample surfaces after annealing were less oxidized because of the reduction reactions.

According to the Pt−Ti phase diagram, different intermetallic phases, namely, Ti_3Pt, Ti_4Pt_3, α-TiPt, and $TiPt_3$, can be formed during annealing.[52] $TiPt_3$ compound was reported to form during annealing of binary Pt/Ti films in the temperature range of 750−800 °C.[47,53] However, given that titanium has a very high affinity to oxygen, in order for Pt to react with Ti in the TiCaPCON−Pt films, the TiO_2 reduction reaction should be promoted.

Usually, Pt NPs located onto the TiO_2 surface readily adsorb carbon monoxide and hydrogen. These chemisorption properties, however, were not observed after reduction at high temperatures because of strong metal−support interaction (SMSI).[54] The migration of reduced species from the TiO_2 is accompanied by the formation of Pt−Ti bonds and NP encapsulation.[55,56] SMSI was detected for Pt/TiO_2 above 280 °C with the formation of Pt−Ti−O alloy upon annealing in vacuum.[57] The migration of a Ti suboxide on top of Fe NPs during annealing was also reported.[57] To explain the reduction reaction, it is reasonable to assume that metal NPs are sufficiently reactive to catalyze decomposition $TiO_2 \rightarrow TiO_x + O_{2-x}$. High-energy ion implantation results in the penetration of Pt atoms into TiO_2 crystal lattice, where such atoms can be stabilized as Pt(IV) and Pt(II) species,[58,59] that is, substituting Ti in the TiO_2 lattice or in the surface oxide PtO. The formation of Pt-based clusters within TiO_2 can cause weakly bonded oxygen[60] and facilitate the reduction reaction during annealing. The SMSI led to the reaction of metallic Fe NPs with TiO_2 and formation of mixed Fe/Ti oxides (e.g., $FeTiO_3$).[61] It is well known that metal Pt cannot be oxidized to PtO in the air even at high temperature. Note, however, that during the calcination process at 400 °C, the Pt atoms thermally diffused from Pt particles into the lattice of TiO_2 grains and substitute for Ti^{4+} to form Pt^{2+}.[62] The possible reduction reactions can be expressed as follows:

$$2Ca + TiO_2 \rightarrow 2CaO + Ti \quad (1)$$

$$2Fe + 3TiO_2 \rightarrow 2FeTiO_3 + Ti \quad (2)$$

Film graphitization during annealing can be explained as follows. Hydrogenated CH_x (which observed in the XRS C 1s spectra) can transform into graphitic carbon by losing hydrogen. In the case of Pt/C catalysts, hydrocarbonaceous overlays covering the surface of the catalysts lose hydrogen and transform into graphitic carbon upon evacuation.[63] During thermal annealing, the nanoscale amorphous deposit is subjected to multistage transformation including dehydration (150 °C), dehydrogenation (150−300 °C), graphitization (>350 °C), and formation of nanocrystalline graphitic deposit around 450 °C.[64] Free Ti resulting from reduction reactions 1 and 2 reacts with amorphous carbon and Pt and forms TiC and $PtTi_x$ phases as evidenced by XPS C 1s and Pt 4f spectra.

4.2. ROS Generation. Generally, there was no correlation in our experiments between the maximum amount of ROS and oxygen concentration on the sample surfaces (Table 2). Simultaneously, the presence of NPs is critical for ROS generation. In the case of the NP-free TiCaPCON film, the ROS generation was only observed after UV exposure, but the ROS concentration was low in comparison with the NP-decorated samples. There was a good correlation between the type of the sample and the amount of generated ROS for all three types of experiments (Figure 6), but the maximum ROS concentrations were different: 700−3000 (UV exposure), 400−900 (visible light), and 3−12 (storage in darkness) nmol/cm^2. Different metal−oxide NPs were reported to generate ROS under UV irradiation.[65] Iron nanostructures are known to play an active role in various homogeneous and heterogeneous redox reactions, and iron oxide NPs are highly active for ROS generation. For example, Fe^{2+} easily reacts with H_2O_2 to form hydroxyl radicals ($^{\bullet}OH$) through the classic homogeneous Fenton reaction.[66,67] Different reactions of oxidative radical generation by iron oxide NPs in the biological environment were considered by Wang[68] and Rtimi[69] under sunlight irradiation. The combination of oxidized Fe NPs and TiO_2 could promote intensive ROS generation under UV or visible light absorption. Because of charge separation in semiconductor devices, the photogenerated electrons and holes interact with surface-adsorbed molecules such as water and oxygen to form active radicals.[70] ROS can contribute to total antibacterial activity not only through the induction of oxidative stress but also because of the damage of the biomolecules such as protein and DNA. In addition, the light absorption of TiO_2 component can be improved by appropriate doping, which hinders the photo-generated charge recombinations through the introduction of intragap energy levels midway between the conduction and valence bands of TiO_2, thereby facilitating the indirect transition of electrons trough the forbidden band.[71] In contrast, Pt NPs

DOI: 10.1021/acsami.9b09649
ACS Appl. Mater. Interfaces 2019, 11, 28699−28719

were reported to have the antioxidant capacity and scavenge ROS.[72,73]

In order to investigate the Pt to TiO_2 interaction in more detail, analysis of slabs consisting of TiO_2 (both anatase and rutile) and Pt with minimum mismatch (less 5%) was performed. Because of the relatively large size of Pt NPs observed in our experiments, the Pt/TiO_2 interface was represented as a junction of flat Pt and TiO_2 slabs in a periodic boundary conditions. The charge redistribution between TiO_2 and Pt was calculated using the formula:

$$\rho = \rho(TiO_2/Pt) - \rho(TiO_2) - \rho(Pt) \quad (3)$$

The results indicated that because of the electronegativity difference between the oxygen atoms in TiO_2 and Pt atoms, there is charge redistribution between these slabs (Figure 12).

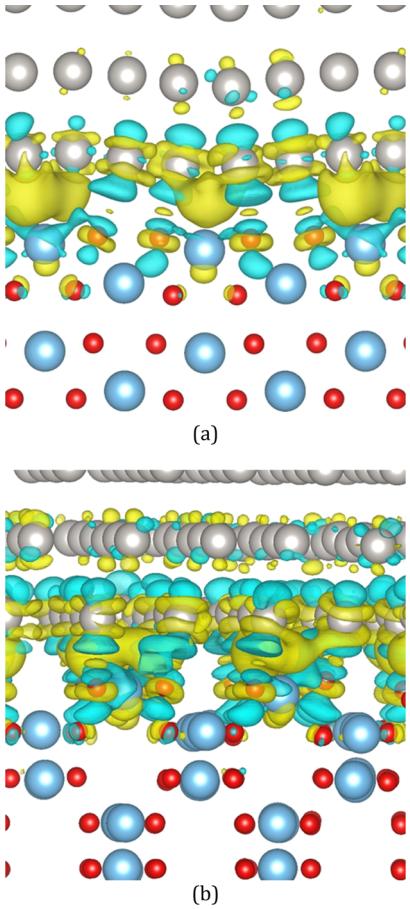

Figure 12. Spatial distribution of electron density difference at TiO_2(rutile)/Pt (a) and TiO_2(anatase)/Pt (b) interfaces. Blue, red, and silver colors correspond to Ti, O, and Pt atoms, respectively. The positive and negative differences are marked by yellow color and turquoise blue clouds, respectively. Isosurface level is 0.004 e/Å.

Strong hybridization between Pt and TiO_2 indicates the formation of strong chemical bonding and conduction channels. Moreover, Bader charge analysis does not show increased charge on the Pt surface in the Pt/TiO_2 structure in comparison with pure Pt slab. The photoexcitation of TiO_2 phase (recall that the samples were sterilized by UV radiation) may lead to the formation of electron–hole pairs[74] according to the following reaction:

$$TiO_2 + h\nu \rightarrow h^+ + e_c^- \quad (4)$$

Pt can capture photogenerated conduction electrons, which are further transferred to electron acceptor H_3O^+:

$$H_3O^+ + e^- \rightarrow {}^\bullet OH + H_2\,(\text{on Pt}) \quad (5)$$

and

$$H_3O^+ + e^- \rightarrow {}^\bullet OH + {}^\bullet H + {}^\bullet H\,(\text{on Pt}) \quad (6)$$

Hydroxyl radicals are highly reactive (easily form hydroxyl groups) and can make significant contribution to the total antibacterial activity of the Pt/TiO_2 couples.

4.3. Factors Affecting Antibacterial Activity. There are three main factors which can impart the antibacterial characteristics of NP-decorated films: (i) ion release, (ii) ROS generation, and (iii) surface microgalvanic couples. Table 8 summarized ion and ROS concentrations (12 and 24 h), as well as potential differences of samples before and after their exposure in NSS for 12 h. These data should be compared with film antibacterial efficiencies (Table 9). The concentration of Pt ions in NSS was very low and for the Pt and $(Pt + Fe)_{an}$ samples was below <4 ppb. As far as we know, the antimicrobial efficacy of Pt in their ionic form was not reported. The minimal inhibitory concentration for Pt ions in solutions against planktonic *P. pneumoniae*, *A. baumannii*, and *E. faecium* strains was found to be 3.9, 5.8, and 11.7 ppm, respectively, but exact bacterial toxicity mechanism was not proposed.[20] As these values are three orders of magnitude higher than those in our experiments, the Pt ion release factor can be excluded.

Microgalvanic processes can significantly affect the film dissolution process in the biological environment, and intermetallic compounds can be of crucial importance for the microgalvanic corrosion behavior. The PtTi intermetallic NPs were the main phase in the Pt-implanted films after annealing. These intermetallic NPs (cathodes) exhibit high potential differences with respect to the matrix (up to 30 mV). For example, during exposure of $(Pt + Fe)_{an}$ sample in NSS, the potential difference reached 60 mV. Such surfaces can kill bacteria upon contact and, therefore, are promising as a nonantibiotic-based surface to fight bacterial infections. Under physiological conditions, the Gram-positive and Gram-negative bacterial cell surface carries negative charge that originates from dissociation or protonation of carboxyl (−COOH), phosphate ($-HPO_4$, $-H_2PO_4$, $-HPO_4^-$), and amino (NH_3^+) groups. The bacteria are very sensitive to changes of environmental conditions, in particular pH, through adsorption of ions and macromolecular components.[75] Upon approach of a charged implant surface, charged groups may associate or dissociate on the surface of bacteria changing their conformation. The most common mechanism of bacterial adhesion is the electrostatic interaction between bacteria and the implant surface.[76,77] To verify the microgalvanic hypothesis further, additional model tests were carried out to minimize the ROS generation contribution. Five selected samples were preliminarily immersed in NSS for 24 h and then subjected to antibacterial test toward *E. coli* U20 strains (Figure 13). After 8 h, a noticeable antibacterial effect was observed, which increased in the following sequence Pt (70%) → Pt_{an} (89%) and Pt + Fe (89%) → $(Pt + Fe)_{an}$ (97%) → Fe_{an} (98%). Before discussing the results, we should highlight that after sample exposure in NSS for 24 h, the Pt and Fe ion release in the next 8 h was almost completely suppressed (except Pt_{an} sample in which the weak ion leaching continued, Figure 5a,b). Additional ROS generation tests were performed under similar antibacterial test conditions. After corresponding

DOI: 10.1021/acsami.9b09649
ACS Appl. Mater. Interfaces 2019, 11, 28699−28719

Table 8. Physical and Chemical Characteristics of Samples Immersed in NSS

sample	ion release, ppb				ROS, nmol/L (UV irradiation)		NP-matrix potential difference, mV	
	Pt		Fe					
	12 h	24 h	12 h	24 h	12 h	24 h	0 h	12 h
Fe			1850	2145			15−30	
Fe_{an}			1000	1210	1310	910	25−30	
Pt	1	1			320	300		
Pt_{an}	8	12			1700	730	15−30	30−40
Pt + Fe	18	18	1150	1440	2230	305	25−30	40−50
$(Pt + Fe)_{an}$	4	5	1645	1900	985	170	25−35	40−50
Pt_{an} + Fe	18	24	1850	1915	1970	310		20−40

Table 9. Antibacterial Efficiency[a]

sample	antibacterial effect, log-reduction										
	E. coli K261		*K. pneumoniae* B1079k/17-3	*A. baumannii* B1280A/17	*S. aureus* no. 839		*S. epidermidis* i5189-1	*E. faecium* Ya-235 : VanA	*E. faecium* I-237: VanA	*E. coli* U20	
	8 h	24 h	24 h	24 h	8 h	24 h	24 h	24 h	24 h	8 h	24 h
Pt	0	0			0					2/4	4
Pt_{an}	0	0	0	0	0	−/4	0	2	0	2/2	2/2
Fe	1/4*	1/4	4	4	4/4	−/4		4	4	2	4/0
Fe_{an}	0	0			4					1/4	4
Pt + Fe	0	0			4					2/2	4
Pt_{an} + Fe	0.5	1/0	3	3	1	4	4	0	2	1	4/4
$(Pt + Fe)_{an}$	0	0	0	0	2			0.5	2	2/4	3

[a]/* different tests.

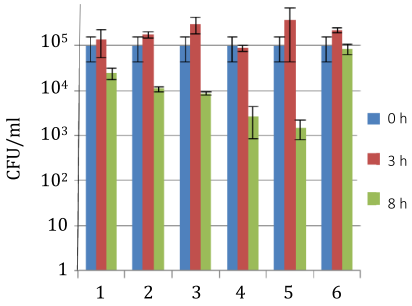

Figure 13. Antibacterial activity of samples against the *E. coli* U20 strains after their preliminary exposure in NSS for 24 h. 1—Pt, 2—Pt_{an}, 3—Pt + Fe, 4—$(Pt + Fe)_{an}$, 5—Fe_{an}, and 6—control (TiCaPCON film without NPs on its surface).

treatment, the samples were preliminarily immersed in NSS for 24 h, then the solution was replaced with a new one, and finally the ROS concentration was measured after 8 h (Figure 6). The ROS concentration was 18−38 nmol/cm^2 that was significantly lower than the ROS amount generated by the TiCaPCON film after UV irradiation (450 nmol/cm^2). As the TiCaPCON sample was used as a control with no antibacterial effect, this ROS concentration level can be considered safe. Thus, the ROS contribution to the total antibacterial activity after sample immersion in NSS for 24 h can be completely excluded. This indicates an important role of sample surfaces in bacterial inactivation even as ROS concentration is low. The resistivity value of TiCaPCON film was reported to be low, 29 Ω/cm^2, which is typical for conductive materials.[22] The NP/matrix potential difference was well documented by the Kelvin probe method for all films except Pt. This is, however, more likely because of a lack of method sensitivity, rather than because of the absence of potential difference (a slight potential contrast can be seen between single Pt NPs and the surrounding matrix shown in Figure 7d). Thus, eliminating the contribution of ions and ROS, we have clearly demonstrated, for the first time, that bacteria can be killed through direct microgalvanic interaction.

The possibility of microgalvanic currents was further supported by BE calculations. Strong bonding at the interface is important for electrochemical processes and charge transfer. For example, the enhanced electrocatalytic activity of TiC-, TiCN-, and TiN-supported Pt NPs toward CO oxidation in alkaline and acidic media was attributed to a negative charge transfer from the support to Pt NPs. This can lead to the formation of electron-enriched Pt sites that affect the adsorption of species.[78] To study the interfaces between these phases and Pt, the atomic models of Pt/TiC, Pt/TiN, and Pt/TiCN structures were considered (Figure 14). It was found that the value of BE varies from 0.29 eV/Å^2 for the Pt/TiN to 0.51 eV/Å^2 for the Pt/TiC and to 0.41 eV/Å^2 for the Pt/TiCN interfaces. Thus, the occurrence of microgalvanic currents at the Pt/TiC(N) interfaces in the biological solution is quite possible. For the sake of completeness note, the galvanic effects on bacterial inactivation were systematically studied in the literature. For example, Cao et al.[79,80] were the first who suggested the possibility of bacterial inactivation due to microgalvanic effect. They studied Ti samples doped with Ag and Zn, whereas both elements are bactericides. However, the authors had abandoned their hypothesis in a later publication, focusing on the assumption that the oxidative stress is the main bacteria killing mechanism.[81] Utilization of porinless *E. coli* allowed to demonstrate that leaching of bactericide Ag and Cu ions is not the only reason for bacterial inactivation, which was additionally assisted by surface contact effects under low-intensity actinic light irradiation.[82] The interfacial charge-transfer mechanism between CuO and Ag_2O was suggested based on the electron−hole pair separation under the irradiation.

DOI: 10.1021/acsami.9b09649
ACS Appl. Mater. Interfaces 2019, 11, 28699−28719

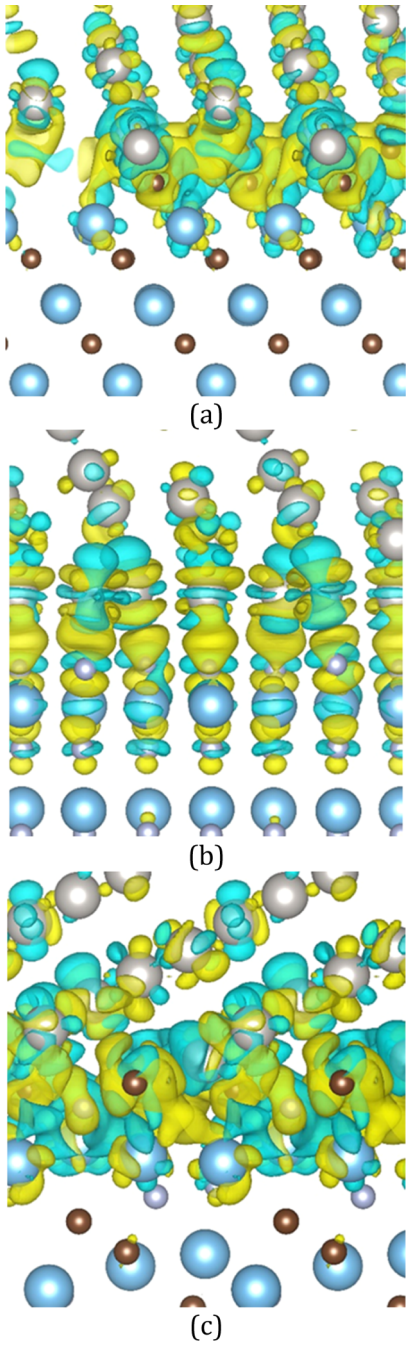

Figure 14. Spatial distribution of electron density difference at Pt/TiC (a), Pt/TiN (b), and Pt/TiCN (c) interfaces. Blue, gray, small silver, and big silver colors correspond to Ti, C, N, and Pt atoms, respectively. The positive and negative differences are marked by yellow and turquoise blue clouds, respectively. The isosurface level is 0.004 e/Å.

For further discussion of the antibacterial mechanisms, it is worth noting that Pt, Fe, and $PtTi_x$ NP-decorated TiCaPCON films are active photocatalysts and generate ROS under visible light and UV irradiation. In the present study, all samples were sterilized by UV radiation, which led to the generation of large amounts of ROS. As no bactericidal effect was observed in the case of the TiCaPCON film, which was used as a control, the photocatalytic activity of the TiO_2 component can be considered insignificant. Nobel metal/TiO_2 composites usually demonstrate good antibacterial activity when excited under UV irradiation because of surface plasmon resonance effect but are less effective in the dark. Zhang et al.[83] showed that Au/TiO_2 nanocomposites exhibited antibacterial effect because of ROS ($^{\bullet}OH$) produced by the photocatalytic effect under visible light. Li et al.[84] demonstrated that Au/TiO_2 nanocomposites can partly destroy *S. aureus* and *E. coli* cells in darkness. It was assumed that Ag and Au NPs in Ag/TiO_2[85] and Au/TiO_2[86] nanocomposites can capture electrons forming the Schottky barrier at the metal/ceramic interface. It was suggested that the physical contact of bacteria with metallic NPs can result in the electron transfer from the bacteria to the plasmonic NPs and further to the TiO_2 support.[84,86] The further mechanism behind bacterial inactivation is not clear yet. The bacteria can die because of the loss of electrons, as suggested by Wang et al.,[86] or because of the ROS formation that attacks the cell membrane and destroys its integrity.[87] Note that since the bacterial membranes have different thicknesses and charges, their response to the nanocomposite surface can also be different.[88] Finally, note that the surface to bacteria interaction is a combination of complex chemical and biological processes and their understanding requires decoupling of the possible mechanisms with carefully planned and detailed experiments.

5. CONCLUSIONS

Herein, seven types of TiCaPCON-supported Pt and Fe metal NPs and their combinations [denoted as Pt, Fe, Pt + Fe, Pt_{an}, Fe_{an}, Pt_{an} + Fe, and $(Pt + Fe)_{an}$] were fabricated by a combination of magnetron sputtering, metal ion implantation, and vacuum annealing to address an important issue of their antibacterial activity toward eight types of bacterial strains and to uncover related mechanisms taking into account the following factors: (i) surface chemistry, (ii) ion release, (iii) generation of ROS, (iv) potential difference and polarity change between NPs and the surrounding matrix in NSS, (v) formation of microgalvanic couples on the sample surfaces, and (vi) contribution of a passive oxide layer, formed on the surface of films, to general kinetics of the NP dissolution. The most important findings can be summarized as follows.

1. During metal ion implantation and subsequent annealing, the chemistry of sample surface was significantly changed: (i) Pt interacted with Ti to form PtTi intermetallic compounds, (ii) annealing in vacuum led to Pt_{an}, Fe_{an}, and $(Pt + Fe)_{an}$ film graphitization, (iii) in the presence of Fe or Pt NPs, the sample surfaces were less oxidized after annealing.
2. Ion release was highly dependent on the sample surface states. The Pt and Fe ion release rate depended on various factors such as (i) existence of active surface cathodes, (ii) potential differences between NPs and surrounding matrix, and (iii) "dragging" effect when the actively dissolving Fe dragged along some Pt ions.
3. The TiCaPCON films decorated with Pt- and Fe-based NPs are active photocatalysts and generate ROS under exposure to UV and visible light.
4. The formation of strong chemical bonding at the interfaces between Pt and TiO_2 (anatase, rutile), TiC, TiN, and TiCN components as an important parameter for charge redistribution was demonstrated using density functional theory calculations.
5. NP-decorated samples exhibited a strong antibacterial effect against *E. coli* U20 and *S. aureus* no. 839 strains (except Pt). Only Fe and Pt_{an} + Fe samples were effective toward antibiotic-resistant *E. coli* K261 cells. Four

DOI: 10.1021/acsami.9b09649
ACS Appl. Mater. Interfaces 2019, 11, 28699−28719

samples, Fe, Pt_{an}, Pt_{an} + Fe, and $(Pt + Fe)_{an}$, were tested against eight types of bacteria. The $(Pt + Fe)_{an}$ films additionally inactivated *E. faecium* Ya-235: VanA and I-237: VanA strains. The Fe and Pt_{an} + Fe films inhibited the growth of *K. pneumoniae* B1079k/17-3, *A. baumannii* B1280A/17, and *E. faecium* I-237: VanA strains. These two samples also showed 99.9 and 100% antibacterial activity toward *S. epidermidis* i5189-1 (Pt_{an} + Fe) and *E. faecium* Ya-235: VanA (Fe), respectively.

6. An important role of sample surfaces in bacterial inactivation was demonstrated. The potential difference between NPs and the surrounding matrix was well documented by the Kelvin probe method. Eliminating the potential contribution of ions and ROS, we have demonstrated, for the first time, that bacteria can be killed through direct microgalvanic interactions.
7. The Pt- and Fe-doped samples did not affect the viability and proliferation activity of lymphocytes, that is, non-specific activation of cells in the presence of NPs did not occur, and NPs had no any notable effect on the ability of lymphocytes to activate in response to a mitogen.

■ ASSOCIATED CONTENT

Supporting Information

The Supporting Information is available free of charge on the ACS Publications website at DOI: 10.1021/acsami.9b09649.

Full survey XPS spectra of Fe, Fe_{an}, Pt, and Pt_{an} samples before and after exposure in NSS for 24 h; XPS C 1s, Pt 4f, and Ti 2p spectra of Fe, Fe_{an}, and Pt_{an} + Fe samples and their curve-fitting; XPS N 1s, O 1s, and C 1s spectra of Pt, Pt_{an}, Pt + Fe, $(Pt + Fe)_{an}$, Pt_{an} + Fe and their curve-fitting, respectively; XPS Pt 4f, Ti 2p, N 1s, and O1s and their curve-fitting after samples immersion in NSS for 24 h, respectively; Ca, P, and Ti ions released into NSS over time; SR-IR spectra; concentration of ROS in aliquots collected after 12 and 24 h and stored for 54 and 66 h, respectively; AFM height profile and corresponding Kelvin probe force microscopy images of the samples with Fe and Fe_{an} NPs on their surface; antibacterial activity of samples against *E. coli* U20; and antibacterial activity of $(Pt + Fe)_{an}$ samples against *E. faecium* Ya-235: VanA, *E. faecium* I-237: VanA, *K. pneumoniae* B1079k/17-3, *A. baumannii* B1280A/17, and *E. coli* K261 (PDF)

■ AUTHOR INFORMATION

Corresponding Author

*E-mail: shtansky@shs.misis.ru.

ORCID

Elizaveta S. Permyakova: 0000-0003-2581-0803

Dmitry V. Shtansky: 0000-0001-7304-2461

Author Contributions

V.A.P. run coating deposition experiments; A.N.S. performed electrochemical characterization; E.S.P. studied the bactericide ion release and the formation of ROS; A.A.V. analyzed the data and edited the paper; J.L. and D.B. carried out atomic force microscopy, Kelvin probe force microscopy, and Raman characterization and performed analysis of the data; A.M.M. analyzed and interpreted the XPS data; M.M. obtained XPS spectra; P.V.S. studied biofilm formation, V.V.F. performed immunological tests, S.G.I. carried out antibacterial studies; I.V.C. and Z.I.P. performed theoretical modeling; and D.V.S. designed the experiments, analyzed the data, and wrote the paper.

Notes

The authors declare no competing financial interest.

■ ACKNOWLEDGMENTS

The work was supported by the Ministry of Education and Science of the Russian Federation (Increase Competitiveness Program of NUST "MISIS" no. K2-2018-012). M.M. is thankful for the financial support provided by the Ministry of Education, Youth and Sports of the Czech Republic (MEYS CR) under the project CEITEC 2020 (LQ1601) running in the frame of the National Sustainability Program II and is also grateful to CEITEC Nano Research Infrastructure for providing XPS facility supported via MEYS CR (ID LM2015041, 2016−2019). S.G.I., P.V.S., and V.V.F. is thankful to Rospotrebnadzor. The authors are grateful to A. C. Pinchuk and M. V. Silkina for the help with immunological tests.

■ REFERENCES

(1) Raphel, J.; Holodniy, M.; Goodman, S. B.; Heilshorn, S. C. Multifunctional Coatings to Simultaneously Promote Osseointegration and Prevent Infection of Orthopaedic Implants. *Biomaterials* **2016**, *84*, 301−314.

(2) Harrasser, N.; Jüssen, S.; Obermeir, A.; Kmeth, R.; Stritzker, B.; Gollwitzer, H.; Burgkart, R. Antibacterial Potency of Different Deposition Methods of Silver and Copper Containing Diamond-Like Carbon Coated Polyethylene. *Biomater. Res.* **2016**, *20*, 17.

(3) Rau, J. V.; Curcio, M.; Raucci, M. G.; Barbaro, K.; Fasolino, I.; Teghil, R.; Ambrosio, L.; De Bonis, A.; Boccaccini, A. R. Cu-Releasing Bioactive Glass Coatings and Their in Vitro Properties. *ACS Appl. Mater. Interfaces* **2019**, *11*, 5812−5820.

(4) Brobbey, K. J.; Haapanen, J.; Mäkelä, J. M.; Gunell, M.; Eerola, E.; Rosqvist, E.; Peltonen, J.; Saarinen, J. J.; Tuominen, M.; Toivakka, M. Effect of Plasma Coating on Antibacterial Activity of Silver Nanoparticles. *Thin Solid Films* **2019**, *672*, 75−82.

(5) Nastulyavichus, A.; Kudryashov, S.; Smirnov, N.; Saraeva, I.; Rudenko, A.; Tolordava, E.; Ionin, A.; Romanova, Y.; Zayarny, D. Antibacterial Coatings of Se and Si Nanoparticles. *Appl. Surf. Sci.* **2019**, *469*, 220−225.

(6) Sukhorukova, I. V.; Sheveyko, A. N.; Kiryukhantsev-Korneev, Ph. V.; Anisimova, N. Y.; Gloushankova, N. A.; Zhitnyak, I. Y.; Benesova, J.; Amler, E.; Shtansky, D. V. Two Approaches to Form Antibacterial Surface: Doping with Bactericidal Element vs Drug Loading. *Appl. Surf. Sci.* **2015**, *330*, 339−350.

(7) Kaur, R.; Liu, S. Antibacterial surface design - Contact kill. *Prog. Surf. Sci.* **2016**, *91*, 136−153.

(8) Sukhorukova, I. V.; Sheveyko, A. N.; Manakhov, A.; Zhitnyak, I. Y.; Gloushankova, N. A.; Denisenko, E. A.; Filippovich, S. Y.; Ignatov, S. G.; Shtansky, D. V. Synergistic and Long-Lasting Antibacterial Effect of Antibiotic-Loaded TiCaPCON-Ag Films Against Pathogenic Bacteria and Fungi. *Mater. Sci. Eng., C* **2018**, *90*, 289−299.

(9) Modaresifar, K.; Azizian, S.; Ganjian, M.; Fratila-Apachitei, L. E.; Zadpoor, A. A. Bactericidal Effects of Nanopatterns: A Systematic Review. *Acta Biomater.* **2019**, *83*, 29−36.

(10) Elbourne, A.; Crawford, R. J.; Ivanova, E. P. Nano-Structured Antimicrobial Surfaces: From Nature to Synthetic Analogues. *J. Colloid Interface Sci.* **2017**, *508*, 603−616.

(11) Sukhorukova, I. V.; Sheveyko, A. N.; Shvindina, N. V.; Denisenko, E. A.; Ignatov, S. G.; Shtansky, D. V. Approaches for Controlled Ag^+ Ion Release: Influence of Surface Topography, Roughness, and Bactericide Content. *ACS Appl. Mater. Interfaces* **2017**, *9*, 4259−4271.

(12) Linklater, D. P.; De Volder, M.; Baulin, V. A.; Werner, M.; Jessl, S.; Golozar, M.; Maggini, L.; Rubanov, S.; Hanssen, E.; Juodkazis, S.; Ivanova, E. P. High Aspect Ratio Nanostructures Kill Bacteria *via*

DOI: 10.1021/acsami.9b09649
ACS Appl. Mater. Interfaces 2019, 11, 28699−28719

Storage and Release of Mechanical Energy. *ACS Nano* **2018**, *12*, 6657−6667.
(13) Hasan, J.; Crawford, R. J.; Ivanova, E. P. Antibacterial Surfaces: the Quest for a New Generation of Biomaterials. *Trends Biotechnol.* **2013**, *31*, 295−304.
(14) Ferraris, S.; Spriano, S. Antibacterial Titanium Surfaces for Medical Implants. *Mater. Sci. Eng., C* **2016**, *61*, 965−978.
(15) Chouirfa, H.; Bouloussa, H.; Migonney, V.; Falentin-Daudré, C. Review of Titanium Surface Modification Techniques and Coatings for Antibacterial Applications. *Acta Biomater.* **2019**, *83*, 37−54.
(16) Antoci, V., Jr.; Adams, C. S.; Parvizi, J.; Ducheyne, P.; Shapiro, I. M.; Hickok, N. J. Covalently Attached Vancomycin Provides a Nanoscale Antibacterial Surface. *Clin. Orthop. Relat. Res.* **2007**, *461*, 81−87.
(17) Antoci, V., Jr.; Adams, C. S.; Parvizi, J.; Davidson, H. M.; Composto, R. J.; Freeman, T. A.; Wickstrom, E.; Ducheyne, P.; Jungkind, D.; Shapiro, I. M.; Hickok, N. J. The Inhibition of Staphylococcus Epidermidis Biofilm Formation by Vancomycin-Modified Titanium Alloy and Implications for the Treatment of Periprosthetic Infection. *Biomaterials* **2008**, *29*, 4684−4690.
(18) Hickok, N. J.; Shapiro, I. M. Immobilized Antibiotics to Prevent Orthopaedic Implant Infections. *Adv. Drug Delivery Rev.* **2012**, *64*, 1165−1176.
(19) Sukhorukova, I. V.; Sheveyko, A. N.; Kiryukhantsev-Korneev, P. V.; Zhitnyak, I. Y.; Gloushankova, N. A.; Denisenko, E. A.; Filippovich, S. Y.; Ignatov, S. G.; Shtansky, D. V. Toward Bioactive Yet Antibacterial Surfaces. *Colloids Surf., B* **2015**, *135*, 158−165.
(20) Vaidya, M. Y.; McBain, A. J.; Butler, J. A.; Banks, C. E.; Whitehead, K. A. Antimicrobial Efficacy and Synergy of Metal Ions Against Enterococcus Faecium, Klebsiella Pneumoniae and Acinetobacter Baumannii in Planktonic and Biofilm Phenotypes. *Sci. Rep.* **2017**, *7*, 5911.
(21) Litovchenko, N. V.; Potanin, A. Y.; Zamulaeva, E. I.; Sukhorukova, I. V.; Pogozhev, Y. S.; Gloushankova, N. A.; Ignatov, S. G.; Levashov, E. A.; Shtansky, D. V. Combustion Synthesis in the Ti-C-Co-$Ca_3(PO_4)_2$-Ag-Mg System and Application of the Produced Electrodes for Pulsed Electrospark Deposition of a Bioactive Coating Having an Antibacterial Effect. *Surf. Coat. Technol.* **2017**, *309*, 75−85.
(22) Ponomarev, V. A.; Sukhorukova, I. V.; Sheveyko, A. N.; Permyakova, E. S.; Manakhov, A. M.; Ignatov, S. G.; Gloushankova, N. A.; Zhitnyak, I. Y.; Lebedev, O. I.; Polčak, J.; Kozmin, A. M.; Shtansky, D. V. Antibacterial Performance of TiCaPCON Films Incorporated with Ag, Pt, and Zn: Bactericidal Ions Versus Surface Microgalvanic Interactions. *ACS Appl. Mater. Interfaces* **2018**, *10*, 24406−24420.
(23) Jaishankar, M.; Tseten, T.; Anbalagan, N.; Mathew, B. B.; Beeregowda, K. N. Toxicity, Mechanism and Health Effects of Some Heavy Metals. *Interdiscip. Toxicol.* **2014**, *7*, 60−72.
(24) Mosby, C. V.; Glanze, W. D.; Anderson, K. N. *Mosby Medical Encyclopedia*, Revised Edition; The Signet: St. Louis, 1996.
(25) Zheng, Y. F.; Zhang, B. B.; Wang, B. L.; Wang, Y. B.; Li, L.; Yang, Q. B.; Cui, L. S. Introduction of Antibacterial Function into Biomedical TiNi Shape Memory Alloy by the Addition of Element Ag. *Acta Biomater.* **2011**, *7*, 2758−2767.
(26) Ilić, V.; Šaponjić, Z.; Vodnik, V.; Potkonjak, B.; Jovančić, P.; Nedeljković, J.; Radetić, M. The Influence of Silver Content on Antimicrobial Activity and Color of Cotton Fabrics Functionalized with Ag Nanoparticles. *Carbohydr. Polym.* **2009**, *78*, 564−569.
(27) Shtansky, D. V.; Levashov, E. A.; Batenina, I. V.; Gloushankova, N. A.; Anisimova, N. Y.; Kiselevsky, M. V.; Reshetov, I. V. Recent Progress in the Field of Multicomponent Bioactive Nanostructured Films. *RSC Adv.* **2013**, *3*, 11107−11115.
(28) Wardman, P. Fluorescent and Luminescent Probes for Measurement of Oxidative and Nitrosative Species in Cells and Tissues: Progress, Pitfalls, and Prospects. *Free Radicals Biol. Med.* **2007**, *43*, 995−1022.
(29) LeBel, C. P.; Ischiropoulos, H.; Bondy, S. C. Evaluation of the Probe 2′,7′-Dichiorofluorescin as an Indicator of Reactive Oxygen Species Formation and Oxidative Stress. *Chem. Res. Toxicol.* **1992**, *5*, 227−231.
(30) Kalyanaraman, B.; Darley-Usmar, V.; Davies, K. J. A.; Dennery, P. A.; Forman, H. J.; Grisham, M. B.; Mann, G. E.; Moore, K.; Roberts, L. J.; Ischiropoulos, H. Measuring Reactive Oxygen and Nitrogen Species with Fluorescent Probes: Challenges and Limitations. *Free Radical Biol. Med.* **2012**, *52*, 1−6.
(31) Hohenberg, P.; Kohn, W. Inhomogeneous Electron Gas. *Phys. Rev.* **1964**, *136*, B864−B871.
(32) Kohn, W.; Sham, L. J. Self-Consistent Equations Including Exchange and Correlation Effects. *Phys. Rev.* **1965**, *140*, A1133−A1138.
(33) Blöchl, P. E. Projector Augmented-Wave Method. *Phys. Rev. B* **1994**, *50*, 17953−17979.
(34) Kresse, G.; Joubert, D. From Ultrasoft Pseudopotentials to the Projector Augmented-Wave Method. *Phys. Rev. B* **1999**, *59*, 1758−1775.
(35) Kresse, G.; Hafner, J. Ab initiomolecular dynamics for liquid metals. *Phys. Rev. B* **1993**, *47*, 558−561.
(36) Kresse, G.; Hafner, J. Ab initiomolecular-dynamics simulation of the liquid-metal-amorphous-semiconductor transition in germanium. *Phys. Rev. B* **1994**, *49*, 14251−14269.
(37) Kresse, G.; Furthmüller, J. Efficient iterative schemes forab initiototal-energy calculations using a plane-wave basis set. *Phys. Rev. B* **1996**, *54*, 11169−11186.
(38) Perdew, J. P.; Burke, K.; Ernzerhof, M. Generalized Gradient Approximation Made Simple. *Phys. Rev. Lett.* **1996**, *77*, 3865−3868.
(39) Monkhorst, H. J.; Pack, J. D. Special Points for Brillouin-Zone Integrations. *Phys. Rev. B* **1976**, *13*, 5188−5192.
(40) Björkman, T. Van Der Waals Density Functional for Solids. *Phys. Rev. B* **2012**, *86*, 165109.
(41) Tang, W.; Sanville, E.; Henkelman, G. A Grid-Based Bader Analysis Algorithm without Lattice Bias. *J. Phys.: Condens. Matter* **2009**, *21*, 084204.
(42) Momma, K.; Izumi, F. *VESTA 3* for Three-Dimensional Visualization of Crystal, Volumetric and Morphology Data. *J. Appl. Crystallogr.* **2011**, *44*, 1272−1276.
(43) Nosé, Y.; Kushida, A.; Ikeda, T.; Nakajima, H.; Tanaka, K.; Numakura, H. Re-examination of Phase Diagram of Fe-Pt System. *Mater. Trans.* **2003**, *44*, 2723−2731.
(44) Estrade-Szwarckopf, H.; Rousseau, B. U.P.S. and X.P.S. Studies of Alkali-Graphite Intercalation Compounds. *Synth. Met.* **1988**, *23*, 191−198.
(45) Takahagi, T.; Ishitani, A. XPS Study on the Surface Structure of Carbon Fibers using Chemical Modification and C1s Line Shape Analysis. *Carbon* **1988**, *26*, 389−395.
(46) Ferrari, A. C.; Robertson, J. Interpretation of Raman Spectra of Disordered and Amorphous Carbon. *Phys. Rev. B* **2000**, *61*, 14095−14107.
(47) Weng, S.; Qiao, L.; Wang, P. Thermal Stability of Pt-Ti Bilayer Films Annealing in Vacuum and Ambient Atmosphere. *Appl. Surf. Sci.* **2018**, *444*, 721−728.
(48) Zobell, C. E. The Effect of Solid Surfaces upon Bacterial Activity. *J. Bacteriol.* **1943**, *46*, 39−56.
(49) Ivanova, E. P.; Hasan, J.; Webb, H. K.; Gervinskas, G.; Juodkazis, S.; Truong, V. K.; Wu, A. H. F.; Lamb, R. N.; Baulin, V. A.; Watson, G. S.; Watson, J. A.; Mainwaring, D. E.; Crawford, R. J. Bactericidal Activity of Black Silicon. *Nat. Commun.* **2013**, *4*, 2838.
(50) Coughenour, C.; Stevens, V.; Stetzenbach, L. D. An Evaluation of Methicillin-Resistant Staphylococcus Aureus Survival on Five Environmental Surfaces. *Microb. Drug Resist.* **2011**, *17*, 457−461.
(51) Jiao, Q.; Li, L.; Mu, Q.; Zhang, Q. Immunomodulation of Nanoparticles in Nanomedicine Applications. *BioMed Res. Int.* **2014**, *2014*, 426028.
(52) Biggs, T.; Cornish, L. A.; Witcomb, M. J.; Corie, M. B. Revised Phase Diagram for the Pt−Ti System from 30 to 60 at.% Platinum. *J. Alloys Compd.* **2004**, *375*, 120−127.
(53) Ehrlich, A.; Weiß, U.; Hoyer, W.; Geßner, T. Microstructural changes of Pt/Ti bilayer during annealing in different atmospheres - an XRD study. *Thin Solid Films* **1997**, *300*, 122−130.

DOI: 10.1021/acsami.9b09649
ACS Appl. Mater. Interfaces 2019, 11, 28699−28719

(54) Tauster, S. J.; Fung, S. C.; Garten, R. L. Strong Metal-Support Interactions. Group 8 Noble Metals Supported on Titanium Dioxide. *J. Am. Chem. Soc.* **1978**, *100*, 170−175.
(55) Pesty, F.; Steinrück, H.-P.; Madey, T. E. Thermal Stability of Pt Films on TiO_2(110): Evidence for Encapsulation. *Surf. Sci.* **1995**, *339*, 83−95.
(56) Ono, L. K.; Yuan, B.; Heinrich, H.; Cuenya, B. R. Formation and Thermal Stability of Platinum Oxides on Size-Selected Platinum Nanoparticles: Support Effects. *J. Phys. Chem. C* **2010**, *114*, 22119−22133.
(57) Pan, J.-M.; Madey, T. E. The Encapsulation of Fe on TiO_2(110). *Catal. Lett.* **1993**, *20*, 269−274.
(58) Kim, S.; Hwang, S.-J.; Choi, W. Visible Light Active Platinum-Ion-Doped TiO_2 Photocatalyst. *J. Phys. Chem. B* **2005**, *109*, 24260−24267.
(59) Hu, Y.; Song, X.; Jiang, S.; Wei, C. Enhanced Photocatalytic Activity of Pt-Doped TiO_2 for NO_x Oxidation both Under UV and Visible Light Irradiation: A Synergistic Effect of Lattice Pt^{4+} and Surface PtO. *Chem. Eng. J.* **2015**, *274*, 102−112.
(60) Mukri, B. D.; Waghmare, U. V.; Hegde, M. S. Platinum Ion-Doped TiO_2: High Catalytic Activity of Pt^{2+} with Oxide Ion Vacancy in $Ti^{4+}_{1-x}Pt^{2+}_xO^{2-}_x$ Compared to Pt^{4+} without Oxide Ion Vacancy in $Ti^{4+}_{1-x}Pt^{4+}_xO_2$. *Chem. Mater.* **2013**, *25*, 3822−3833.
(61) Zhou, S.; Talut, G.; Potzger, K.; Shalimov, A.; Grenzer, J.; Skorupa, W.; Helm, M.; Fassbender, J.; Čižmár, E.; Zvyagin, S. A.; Wosnitza, J. Crystallographically Oriented Fe Nanocrystals Formed in Fe-Implanted TiO_2. *J. Appl. Phys.* **2008**, *103*, 083907.
(62) Li, Q.; Wang, K.; Zhang, S.; Zhang, M.; Yang, J.; Jin, Z. Effect of Photocatalytic Activity of CO Oxidation on Pt/TiO_2 by Strong Interaction Between Pt and TiO_2 Under Oxidizing Atmosphere. *J. Mol. Catal. A: Chem.* **2006**, *258*, 83−88.
(63) Paál, Z.; Wootsch, A. Catalytic Properties of the Platinum-Hydrogen-Carbon System. In *Catalysis in Application*; Jackson, S. D., Hargreaves, J. S. J., Lennon, D., Eds.; Royal Society of Chemistry, 2003, Vol. *289*; pp 8−15
(64) Kulkarni, D. D.; Rykaczewski, K.; Singamaneni, S.; Kim, S.; Fedorov, A. G.; Tsukruk, V. V. Thermally Induced Transformations of Amorphous Carbon Nanostructures Fabricated by Electron Beam Induced Deposition. *ACS Appl. Mater. Interfaces* **2011**, *3*, 710−720.
(65) Li, Y.; Zhang, W.; Niu, J.; Chen, Y. Mechanism of Photogenerated Reactive Oxygen Species and Correlation with the Antibacterial Properties of Engineered Metal-Oxide Nanoparticles. *ACS Nano* **2012**, *6*, 5164−5173.
(66) Urbański, N. K.; Beresewicz, A. Generation of $^{\bullet}OH$ Initiated by Interaction of Fe^{2+} and Cu^{+} with Dioxygen; Comparison with the Fenton Chemistry. *Acta Biochim. Pol.* **2000**, *47*, 951−962.
(67) Wu, H.; Yin, J.-J.; Wamer, W. G.; Zeng, M.; Lo, Y. M. Reactive Oxygen Species-Related Activities of Nano-Iron Metal and Nano-Iron Oxides. *J. Food Drug Anal.* **2014**, *22*, 86−94.
(68) Wang, B.; Yin, J.-J.; Zhou, X.; Kurash, I.; Chai, Z.; Zhao, Y.; Feng, W. Physicochemical Origin for Free Radical Generation of Iron Oxide Nanoparticles in Biomicroenvironment: Catalytic Activities Mediated by Surface Chemical States. *J. Phys. Chem. C* **2013**, *117*, 383−392.
(69) Rtimi, S.; Pulgarin, C.; Sanjines, R.; Kiwi, J. Novel FeOx−Polyethylene Transparent Films: Synthesis and Mechanism of Surface Regeneration. *RSC Adv.* **2015**, *5*, 80203−80211.
(70) Rtimi, S.; Sanjines, R.; Pulgarin, C.; Kiwi, J. Microstructure of Cu-Ag Uniform Nanoparticulate Films on Polyurethane 3D Catheters: Surface Properties. *ACS Appl. Mater. Interfaces* **2016**, *8*, 56−63.
(71) Rtimi, S.; Kiwi, J. Bactericide Effects of Transparent Polyethylene Photocatalytic Films Coated by Oxides Under Visible Light. *Appl. Catal., B* **2017**, *213*, 62−73.
(72) Hamasaki, T.; Kashiwagi, T.; Imada, T.; Nakamichi, N.; Aramaki, S.; Toh, K.; Morisawa, S.; Shimakoshi, H.; Hisaeda, Y.; Shirahata, S. Kinetic Analysis of Superoxide Anion Radical-Scavenging and Hydroxyl Radical-Scavenging Activities of Platinum Nanoparticles. *Langmuir* **2008**, *24*, 7354−7364.
(73) Watanabe, A.; Kajita, M.; Kim, J.; Kanayama, A.; Takahashi, K.; Mashino, T.; Miyamoto, Y. In Vitro Free Radical Scavenging Activity of Platinum Nanoparticles. *Nanotechnology* **2009**, *20*, 455105−455114.
(74) Li, Y.; Xie, Y.; Peng, S.; Lu, G.; Li, S. Photocatalytic Hydrogen Generation in the Presence of Chloroacetic Acids over Pt/TiO_2. *Chemosphere* **2006**, *63*, 1312−1318.
(75) Poortinga, A. T.; Bos, R.; Norde, W.; Busscher, H. J. Electric double layer interactions in bacterial adhesion to surfaces. *Surf. Sci. Rep.* **2002**, *47*, 1−32.
(76) Campoccia, D.; Montanaro, L.; Arciola, C. R. A Review of the Biomaterials Technologies for Infection-Resistant Surfaces. *Biomaterials* **2013**, *34*, 8533−8554.
(77) Rtimi, S.; Dionysiou, D. D.; Pillai, S. C.; Kiwi, J. Advances in Catalytic/Photocatalytic Bacterial Inactivation by Nano Ag and Cu Coated Surfaces and Medical Devices. *Appl. Catal., B* **2019**, *240*, 291−318.
(78) Roca-Ayats, M.; García, G.; Galante, J. L.; Peña, M. A.; Martínez-Huerta, M. V. TiC, TiCN, and TiN Supported Pt Electrocatalysts for CO and Methanol Oxidation in Acidic and Alkaline Media. *J. Phys. Chem. C* **2013**, *117*, 20769−20777.
(79) Cao, H.; Qiao, Y.; Liu, X.; Lu, T.; Cui, T.; Meng, F.; Chu, P. K. Electron Storage Mediated Dark Antibacterial Action of Bound Silver Nanoparticles: Smaller is not Always Better. *Acta Biomater.* **2013**, *9*, 5100−5110.
(80) Cao, H.; Liu, X.; Meng, F.; Chu, P. K. Biological Actions of Silver Nanoparticles Embedded in Titanium Controlled by Micro-Galvanic Effects. *Biomaterials* **2011**, *32*, 693−705.
(81) Wang, G.; Jin, W.; Qasim, A. M.; Gao, A.; Peng, X.; Li, W.; Feng, H.; Chu, P. K. Antibacterial Effects of Titanium Embedded with Silver Nanoparticles Based on Electron-Transfer-Induced Reactive Oxygen Species. *Biomaterials* **2017**, *124*, 25−34.
(82) Rtimi, S.; Nadtochenko, V.; Khmel, I.; Bensimon, M.; Kiwi, J. First Unambiguous Evidence for Distinct Ionic and Surface-Contact Effects during Photocatalytic Bacterial Inactivation on Cu-Ag Films: Kinetics, Mechanism and Energetics. *Mater. Today Chem.* **2017**, *6*, 62−74.
(83) Zhang, J.; Suo, X.; Zhang, J.; Han, B.; Li, P.; Xue, Y.; Shi, H. One-Pot Synthesis of Au/TiO2 Heteronanostructure Composites with SPR Effect and its Antibacterial Activity. *Mater. Lett.* **2016**, *162*, 235−237.
(84) Li, J.; Zhou, H.; Qian, S.; Liu, Z.; Feng, J.; Jin, P.; Liu, X. Plasmonic Gold Nanoparticles Modified Titania Nanotubes for Antibacterial Application. *Appl. Phys. Lett.* **2014**, *104*, 261110.
(85) Prakash, J.; Kumar, P.; Harris, R. A.; Swart, C.; Neethling, J. H.; Van Vuuren, A. J.; Swart, H. C. Synthesis, characterization and multifunctional properties of plasmonic Ag-TiO2nanocomposites. *Nanotechnology* **2016**, *27*, 355707.
(86) Wang, G.; Feng, H.; Gao, A.; Hao, Q.; Jin, W.; Peng, X.; Li, W.; Wu, G.; Chu, P. K. Extracellular Electron Transfer from Aerobic Bacteria to Au Loaded TiO2 Semiconductor without Light: a New Bacteria Killing Mechanism other than Localized Surface Plasmon Resonance or Microbial Fuel Cells. *ACS Appl. Mater. Interfaces* **2016**, *8*, 24509−24516.
(87) Vecitis, C. D.; Zodrow, K. R.; Kang, S.; Elimelech, M. Electronic-Structure-Dependent Bacterial Cytotoxicity of Single-Walled Carbon Nanotubes. *ACS Nano* **2010**, *4*, 5471−5479.
(88) Li, J.; Wang, G.; Zhu, H.; Zhang, M.; Zheng, X.; Di, Z.; Liu, X.; Wang, X. Antibacterial Activity of Large-Area Monolayer Graphene Film Manipulated by Charge Transfer. *Sci. Rep.* **2014**, *4*, 4359.

DOI: 10.1021/acsami.9b09649
ACS Appl. Mater. Interfaces 2019, 11, 28699−28719